

SYNTHESIS AND CHARACTERIZATION OF TITANOSILICATE
ETS-10 FOR POTENTIAL PHOTOVOLTAIC APPLICATIONS

A THESIS SUBMITTED TO
THE GRADUATE SCHOOL OF NATURAL AND APPLIED SCIENCES
OF
MIDDLE EAST TECHNICAL UNIVERSITY

BY

SEZİN GALİOĞLU

IN PARTIAL FULFILLMENT OF THE REQUIREMENTS
FOR
THE DEGREE OF MASTER OF SCIENCE
IN
MICRO AND NANOTECHNOLOGY

JUNE 2010

Approval of the thesis:

SYNTHESIS AND CHARACTERIZATION OF TITANOSILICATE ETS-10 FOR POTENTIAL PHOTOVOLTAIC APPLICATIONS

submitted by **SEZİN GALİOĞLU** in partial fulfillment of the requirements for the degree of **Master of Science in Micro and Nanotechnology Department, Middle East Technical University** by,

Prof. Dr. Canan Özgen
Dean, Graduate School of **Natural and Applied Sciences** _____

Prof. Dr. Zühal Küçükyavuz
Head of Department, **Micro and Nanotechnology** _____

Assist. Prof. Burcu Akata Kurç
Supervisor, **Dept. of Micro and Nanotechnology, METU** _____

Prof. Dr. Mehmet Parlak
Co-Supervisor, **Department of Physics, METU** _____

Examining Committee Members:

Prof. Dr. Macit Özenbaş
Department of Metallurgical and Materials Eng., METU _____

Assist. Prof. Burcu Akata Kurç
Department of Micro and Nanotechnology, METU _____

Prof. Dr. Mehmet Parlak
Department of Physics, METU _____

Prof. Dr. Raşit Turan
Department of Physics., METU _____

Prof. Dr. Hayrettin Yücel
Department of Chemical Eng., METU _____

Date: _____

I hereby declare that all information in this document has been obtained and presented in accordance with academic rules and ethical conduct. I also declare that, as required by these rules and conduct, I have fully cited and referenced all material and results that are not original to this work.

Name, Last Name: SEZİN GALİOĞLU

Signature :

ABSTRACT

SYNTHESIS AND CHARACTERIZATION OF TITANOSILICATE ETS-10 FOR POTENTIAL PHOTOVOLTAIC APPLICATIONS

Galioglu, Sezin

M.Sc., Department of Micro and Nanotechnology

Supervisor : Assist. Prof. Dr. Burcu Akata Kurç

Co-Supervisor: Prof. Dr. Mehmet Parlak

June 2010, 71 Pages

Different kinds of nanoparticles are widely used in optoelectronic and photovoltaic applications to harvest light to increase efficiency of devices. ETS-10, which is a synthetic microporous material consisting of $-Ti-O-Ti-O-Ti-$ wires that run in the crystal in a and b directions, has been of interest in such applications due to its unique properties. In the current study, the synthesis conditions of ETS-10 were investigated in order to obtain pure ETS-10 crystals with the desired morphology. For this purpose, ETS-10 crystals were synthesized using different molar compositions. The effects of several synthesis parameters on the obtained products were investigated.

Furthermore, ETS-10 thin films were prepared on ITO glass substrates using secondary growth of ETS-10 for the first time. The orientation of the -Ti-O-Ti-O-Ti- wires inside ETS-10 were explored by preparing several ETS-10 films on the ITO glass substrates using secondary growth of ETS-10 multilayers with a partial a(b)-out-of-plane preferred crystal orientation. This orientation can be desirable for the advanced applications of ETS-10 films.

Afterwards, silver nanoparticle modified ETS-10 crystals were prepared and characterized in detail to understand the interaction of silver nanoparticles with the synthesized ETS-10 crystals. For this purpose, ETS-10 in the as-prepared and silver nanoparticle containing forms have been characterized using, XRD, ICP-OES, SEM, HR-TEM, N₂ Adsorption, XPS, and UV/VIS spectroscopy. In order to investigate the optical properties of the silver modified ETS-10, transmittance-reflectance measurements were carried out. In general, it is believed that all steps necessary for the preparation of ETS-10 films and preliminary steps for investigating ETS-10 for future photovoltaic applications were determined.

Keywords: ETS-10, Secondary Growth, Silver nanoparticles, XRD, Transmittance-Reflectance.

ÖZ

TİTANYUMSİLİKAT ETS-10'LERİN OLASI FOTOVOLTAİK UYGULAMALAR İÇİN SENTEZLENMESİ VE KARAKTERİZE EDİLMESİ

Galioglu, Sezin

Yüksek Lisans, Mikro ve Nanoteknoloji Bölümü

Tez Yöneticisi : Yrd. Doç. Dr. Burcu Akata Kurç

Ortak Tez Yöneticisi: Prof. Dr. Mehmet Parlak

Haziran 2010, 71 sayfa

Metal nanoparçacıkları, kuantum noktaları ve TiO_2 gibi değişik tipteki nanoparçacıklar optoelektronik ve fotovoltaik uygulamalarda, ışığı toplamak ve optik, elektronik aygıtlarda verimi arttırmak üzere sıkça kullanılırlar. Sentetik mikro-gözenekli titanyumsilikat olan ve içerisinde a ve b yönlerinde uzanan, -Ti-O-Ti-O-Ti- zinciri barındıran ETS-10, mikro-gözenekli yapı ve yarıiletken elektronik özellik gösterme durumlarından dolayı bu tip uygulamalarda ilgi görmektedir. Bu tez çalışmasında, kusur içermeyen saf ve istenilen morfolojide ETS-10 kristalleri elde etmek için, sentez şartları araştırılmıştır. ETS-10 kristalleri bu amaçla farklı molar kompozisyonlardan sentezlenmiştir. Sentezi etkileyen birçok değişik parametre incelenmiştir.

Sentezlenen ETS-10 kristallerin ince filmleri ITO cam alttaşı üzerine ikincil büyütme tekniği kullanılarak ilk kez olarak hazırlanmıştır. İstenilen a(b)-yüzey-

dışı kristal yönelimine sahip ETS-10 filmleri, ETS-10 çok katmanlı ikincil büyütme yöntemi kullanılarak ITO cam üzerine büyütülmüştür ve ETS-10 kristallerinin içindeki -Ti-O-Ti-O-Ti zincirlerinin yönelimlerinin hesaplamaları yapılmıştır. Bu yönelim, ETS-10 filmlerin ileri düzey uygulamaları için istenilen bir özellik olabilir.

Daha sonra, gümüş nanoparçacıkları ile sentezlenen ETS-10 kristallerinin etkileşimleri anlayabilmek için gümüş nanoparçacıkları ile modifiye edilmiş ETS-10 kristalleri hazırlanmış ve detaylı olarak karakterize edilmiştir. Bu amaçla, gümüş nanoparçacıkları içeren ve içermeyen ETS-10 kristalleri X-Işını Kırınım Cihazı (XRD), Endüktif Eşleşmiş Plazma Spektroskopisi (ICP-OES), Taramalı Elektron Mikroskobu (SEM), Tünelleme Elektron Mikroskobu (TEM), N₂ Adsorpsiyon Tekniği, X-Işını Fotoelektron Spektroskopisi (XPS) ve UV/VIS Spektroskopisi kullanılarak karakterize edilmiştir. Gümüş nano parçacıklarla modifiye edilen ETS-10 kristallerinin optik özelliklerini anlayabilmek için, Geçirgenlik-Yansıma ölçümleri yapılmıştır. Bu tez çalışmasında, ETS-10 kristallerinin fotovoltaik uygulamalarda ve gelecek araştırmalardaki olası kullanım alanları için gerekli ilk verilerin alındığına inanılmaktadır.

Anahtar Kelimeler: ETS-10, İkincil Büyütme, Gümüş Nanoparçacıkları, XRD, Geçirgenlik-Yansıma.

to my father...

ACKNOWLEDGEMENTS

It gives me great pleasure to express my sincere gratitude to my advisor Assist. Prof. Burcu Akata Kurç, for her support, inspiration, and guidance during my M.Sc. study. Her trust in me has changed all my academic life.

Furthermore, I would like to thank to the rest of my thesis committee; Prof. Dr. Raşit Turan, Prof. Dr. Mehmet Parlak, Prof. Dr. Hayrettin Yücel, Prof. Dr. Macit Özenbaş for their precious comments.

I would like to thank to group members; Esin Soy, Berna Ozansoy Kasap, Kaan Kirdeciler, Seçkin Öztürk, and Sedat Canlı for their friendship and helps during my study. All of them calmed me down when I was stressed out, and they helped me sincerely when I was in trouble. I would like to thank to Urcan Guler for his great patience and support in the experiments conducted in METU Physics Department. I would also like to thank Prof. Dr. Saim Özkar and Dr. Mehmet Zahmakıran for their guidance and help in the experiments conducted in METU Chemistry Department. I would like to thank Döndü Şahin for her friendship and İlker Yıldız, Ayşe Seyhan, Serap Tekin, Özgür Erişen, and Levent Yıldız for their supports in Central Laboratory. I would like thank Selçuk Yerci for his help about preparation of ITO coated substrates in Boston University. I owe my gratitude to Dr. Juliusz Warzywoda from whom I learned various subjects. Special thanks to Prof. Dr. Albert Sacco Jr. and Mariam N. Ismail for their helps about zeolite synthesis and film preparations conducted in Center for Advanced Microgravity Materials Processing (CAMMP), Department of Chemical Engineering, Northeastern University, Boston, USA.

The author is most grateful to her family members for supporting her continuously throughout her life unconditionally, to her mother, for raising her with never-ending love, patience and support, to her father, for teaching her the excitement of science and committing his life to his family, to her sisters Esin Galioglu and Yeliz Galioglu and to her brother Mehmet Galioglu, for their love, never-ending patience and support. I love you my dear family!

Last but not least, I would like to give my endless gratitude to Emrah Ozaltug, who supported and motivated me with his love and understanding during the whole period of my study.

I am also appreciative of the financial support that I received for this study through Scientific and Technical Research Council of Turkey (TUBITAK) and European Union project with the project number PIRSES-GA-2008-230802.

TABLE OF CONTENTS

ABSTRACT.....	iv
ÖZ	vi
ACKNOWLEDGEMENTS	ix
TABLE OF CONTENTS	xi
LIST OF TABLES	xv
LIST OF FIGURES	xvi
LIST OF SYMBOLS	xix
CHAPTERS	
1. INTRODUCTION	1
1.1 Zeolite and Zeo-type Materials	1
1.1.1 ETS-10	4
1.2 Zeolite and Zeo-type Thin Films	6
1.3 Metal Nanoparticles	7
1.3.1 Preparation Methods of Metal Nanoparticles	7
1.3.2 Surface Plasmon Resonance	9
2. LITERATURE SUMMARY	13

2.1 ETS-10 in Advanced Applications.....	13
2.2 The Preparation of Zeolite and Zeo-type Thin Films	14
2.3 The Application Areas of ETS-10 Containing Silver	15
3. EXPERIMENTAL	17
3.1 ETS-10 Synthesis	17
3.2 Preparation of ETS-10 Thin Films on Indium Tin Oxide	
Surfaces	18
3.2.1 Methods.....	18
3.2.1.1 Secondary Growth	18
3.3 Preparation of ETS-10 Containing Silver Nanoparticles	20
3.3.1 Methods	20
3.3.1.1 Ag ⁺ Ion-exchange and Reduction of Ag ⁺ Ions	20
3.4 Material Characterization.....	21
3.4.1 X-Ray Diffraction (XRD)	21
3.4.2 Scanning Electron Microscopy (SEM)	22
3.4.3 Inductively Coupled Plasma - Optical Emission	
Spectrometry (ICP-OES)	22
3.4.4 UV-VIS Spectroscopy	23
3.4.5 X-Ray Photoelectron Spectroscopy (XPS)	23
3.4.6 Surface and Pore Size Analysis.....	24

3.4.7 Transmission Electron Microscopy (TEM)	24
3.4.8 Transmittance-Reflectance Measurements	25
4. RESULTS AND DISCUSSION	26
4.1 Synthesis of ETS-10.....	26
4.1.1 Effect of Composition and Source Materials	27
4.1.2 Effect of Synthesis Conditions.....	28
4.2 Preparation of ETS-10 Thin Films on Indium Tin Oxide	
Surfaces	33
4.2.1 Methods.....	33
4.2.1.1 Seed Layer Formation.....	33
4.2.1.2 Secondary Growth	36
4.2.2 Microstructural Characterization of ETS-10 Thin Films	37
4.2.2.1 Ti-O-Ti-O-Ti- Wire Orientation and XRD	
Analysis.....	38
4.2.2.2 Morphology of ETS-10 Thin Films	42
4.3 Preparation of ETS-10 Containing Silver Nanoparticles.....	47
4.3.1 Characterization of ETS-10 After Silver Ion-exchange and	
Reduction	47
4.3.1.1 X-Ray Diffraction (XRD) Analysis	47
4.3.1.2 Scanning Electron Microscopy (SEM)	49

4.3.1.3 Inductively Coupled Plasma - Optical Emission Spectrometry (ICP-OES)	51
4.3.1.4 UV-VIS Spectroscopy	52
4.3.1.5 X-Ray Photoelectron Spectroscopy (XPS)	54
4.3.1.6 Surface and Pore Size Analysis.....	55
4.3.1.7 Transmission Electron Microscopy (TEM)	57
4.3.1.8 Transmittance-Reflectance Measurements	59
5. CONCLUSIONS	65
REFERENCES	67

LIST OF TABLES

TABLES

Table 4.1 Summary of ETS-10 synthesis and ETS-10 films trials.	32
Table 4.2 Seed layer thickness, film thickness, columnar grains thickness, and crystallographic preferred orientation index $CPO_{(200)/(105)}$ for ETS-10 films prepared via secondary growth of ETS-10 seed layers deposited using 1, 2, and 3 dip coating steps.	42
Table 4.3 ETS-10 and Ag-ETS-10 Samples and Their Corresponding Na (%), K (%) and Ag (%) Concentration Obtained from ICP-OES Analysis.	51
Table 4.4 Specific Surface Areas of the ETS-10 Samples.....	55
Table 4.5: Textural Characterization Results of ETS-10 and Ag ⁰ -ETS-10.	56

LIST OF FIGURES

FIGURES

Figure 1.1 a) TO_4 Tetrahedra b) TO_4 Tetrahedra sharing a common oxygen vertex [65].	2
Figure 1.2 Primary building blocks of zeolites [64].	3
Figure 1.3 SEM image of ETS-10 crystals.	4
Figure 1.4: Schematic image of ETS-10 crystals [36].	5
Figure 1.5 Crystal structure of polymorph B of ETS-10. a) Typical truncated bipyramidal morphology of the crystals, which consist of a three dimensional network of SiO_2 channels (blue) and TiO_3^{2-} molecular wires (red). b) View along the $[\bar{1}10]$ axis. c) View along the $[110]$ axis. d) A single TiO_3^{2-} molecular wire [50].	5
Figure 1.6 UV/Vis extinction spectra of silver nanoparticle suspensions before (c) and after (c) changes were made to the dielectric environment from A) isopropanol to Teflon AF, B) water to silica, and C) water to titania [53].	11
Figure 1.7 Diagrams depicting the electric field lines of the A) dipole, B) quadrupole, and C) octupole resonances, after ref. [53].	12
Figure 3.1 Schematic illustrating the orientation of the ITO glass substrates in the autoclaves used in the secondary growth step.	19

Figure 4.1 SEM image of secondary growth of ETS-10 using System I.....	29
Figure 4.2: XRD pattern of hydrothermal synthesis of micron-sized ETS-10 using System I. Quartz impurity (red square).....	30
Figure 4.3: XRD pattern of ETS-10 film using System I as a secondary growth solution.	30
Figure 4.4 Top view FE-SEM image of the seed layer deposited using a single dip coating step.	34
Figure 4.5 Top view FE-SEM image of the seed layer deposited using a double dip coating step.	35
Figure 4.6 Top view FE-SEM image of the seed layer deposited using a triple dip coating step.	35
Figure 4.7 FE-SEM image of crystals synthesized in a 2-day unseeded hydrothermal crystallization using the secondary growth mixture.	37
Figure 4.8 XRD patterns of bare ITO glass substrate (a), ETS-10 powder (b), seed layers deposited on the ITO glass substrate using 1 (c), 2 (d), and 3 (e) dip coating steps, and films after secondary growth of seed layers deposited via single (f), double (g), and triple (h) dip coating. The star symbols depict the reflections of the ITO substrate in the patterns of ETS-10 seed layers and films.	39
Figure 4.9 FE-SEM top view (a, c, e) and cross-section (b, d, f) images of ETS-10 films prepared on the ITO glass substrates using secondary growth of seed layers deposited using 1 (a, b), 2 (c, d), and 3 (e, f) dip coating steps. *SL = seed layer, CG = columnar grains.	44
Figure 4.10 XRD patterns of as-synthesized ETS-10 (black), 10%-Ag ⁺ -ETS-10 (red), 93%-Ag ⁺ -ETS-10 (blue), Ag ⁰ -ETS-10 (green).	48

Figure 4.11 SEM images of as-synthesized ETS-10 and ETS-10 containing silver nanoparticles.....	50
Figure 4.12 DR UV-Vis spectra of as-synthesized ETS-10 (black), ion-exchanged ETS-10 (red).	52
Figure 4.13 DR UV-Vis spectra of ETS-10 containing silver nanoparticles. ...	53
Figure 4.14 XPS spectra of ETS-10 containing silver nanoparticles.	54
Figure 4.15 TEM image of ETS-10 containing silver nanoparticles.	57
Figure 4.16 TEM image of ETS-10 containing silver nanoparticles.	58
Figure 4.17: (a) Reflectance data of ETS-10 and Ag ⁰ -ETS-10 samples dip-coated on ITO glass. 1-time (black), 2-times (red), 3-times (blue) dip-coated ETS-10; 1-time (green), 2-times (pink), 3-times (brown) dip-coated Ag ⁰ -ETS-10. (b) Transmittance data of ETS-10 and Ag ⁰ -ETS-10 samples dip-coated on ITO glass. 1-time (black), 2-times (red), 3-times (blue) dip-coated ETS-10; 1-time (green), 2-times (pink), 3-times (brown) dip-coated Ag ⁰ -ETS-10.	60
Figure 4.18: (a) Reflectance data of ETS-10 and Ag ⁰ -ETS-10 samples dip-coated on quartz. 1-time (black), 2-times (red), 3-times (blue) dip-coated ETS-10; 1-time (green), 2-times (pink), 3-times (brown) dip-coated Ag ⁰ -ETS-10. (b) Transmittance data of ETS-10 and Ag ⁰ -ETS-10 samples dip-coated on quartz. 1-time (black), 2-times (red), 3-times (blue) dip-coated ETS-10; 1-time (green), 2-times (pink), 3-times (brown) dip-coated Ag ⁰ -ETS-10.	62

LIST OF SYMBOLS

SPR: Surface Plasmon Resonance

CG: Columnar Grain

SG: Secondary Growth

CPO: Crystallographic Preferred Orientation Index

CHAPTER 1

INTRODUCTION

1.1 Zeolite and Zeo-type Materials

Zeolite and zeolite-like (zeotype) materials with their unique tetrahedral framework structures and compositions, uniform pores, well-defined acidity, cation exchange selectivity, and good thermal stability are widely used as commercial catalysts, ion exchangers, and adsorbents [1].

Zeolite comprises of TO_4 tetrahedra through corner sharing giving rise to a three-dimensional four-connected framework [65]. Framework T atoms generally refer to Si, Al, or P atoms. These $[SiO_4]$, $[AlO_4]$, or $[PO_4]$ tetrahedral are the basic structural building units of a zeolite framework. In a zeolite, each T atom is coordinated to four oxygen atoms (Figure 1.1-a). Each oxygen atom connected two T atoms (Figure 1.1-b).

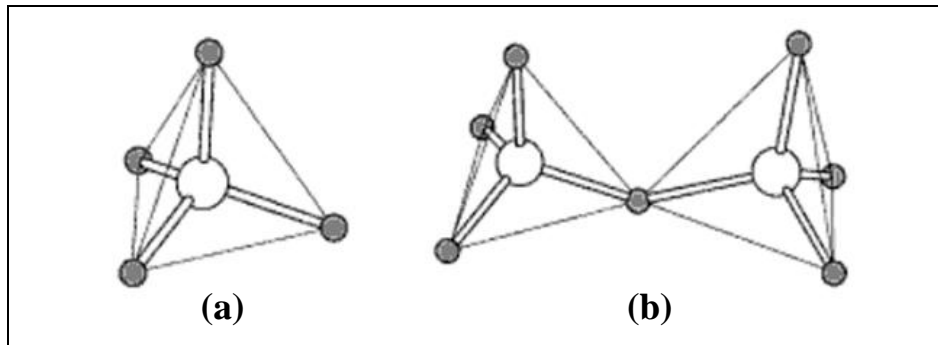


Figure 1.1: a) TO_4 Tetrahedra b) TO_4 Tetrahedra sharing a common oxygen vertex [65].

The aluminosilicate zeolites constructed from SiO_4 tetrahedra and AlO_4 tetrahedra (Figure 1.2) possess an anionic framework, the negative charge of which is compensated by extraframework cations [65]. The empirical formula of an aluminosilicate zeolite can be expressed,

$$\text{A}_{x/n}[\text{Si}_{1-x}\text{Al}_x\text{O}_2] \cdot m\text{H}_2\text{O} \quad (1.1)$$

where A is a metal cation of valence n. The cations and adsorbed water molecules are located in the channels or cages.

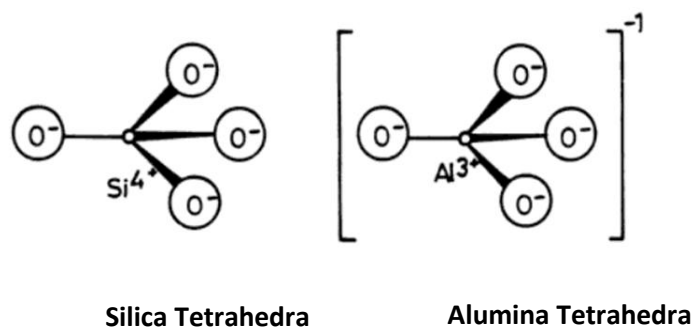


Figure 1.2: Primary building blocks of zeolites [64].

Currently, these as well as other related microporous molecular sieve materials not exclusively formed by tetrahedral units (e.g., microporous titanosilicates with mixed octahedral–tetrahedral frameworks) are being extensively explored for use in advanced applications, such as optoelectronics [2,3], photovoltaics [4–6], and biosensors [7,8]. This is due to their structural/surface features, high surface area, tailored ion exchange capabilities, well-defined cages/channels, transparency in the UV–VIS/NIR region [9–11], and their potential use as host systems for variety of photoactive guests [12,13].

There are an increasing number of investigations involving titanium-containing zeo-type and related microporous titanosilicate molecular sieve materials for optoelectronic, photovoltaic, and photocatalytic applications [3–5, 13, 26–30]. One of these materials is ETS-10.

1.1.1 ETS-10

ETS-10, is a synthetic microporous (pore size $4.9 \times 7.6 \text{ \AA}$) titanosilicate with framework built of corner-sharing TiO_6 octahedra and SiO_4 tetrahedra [31]. These building units are uniquely arranged to form monatomic, linear, orthogonal, non-intersecting, semiconducting $-\text{Ti}-\text{O}-\text{Ti}-\text{O}-\text{Ti}-$ chains that run in the crystal a and b directions as shown in Figure 1.4. These chains are effectively separated from each other by the silica matrix [32] (Figure 1.5), and are regarded as a 1D quantum-confined form of titania with a band gap energy of $\sim 4.03 \text{ eV}$ [33]. Thus, ETS-10 crystals may find potential applications in nanoscale electronic devices [26], and photovoltaic solar cells [4].

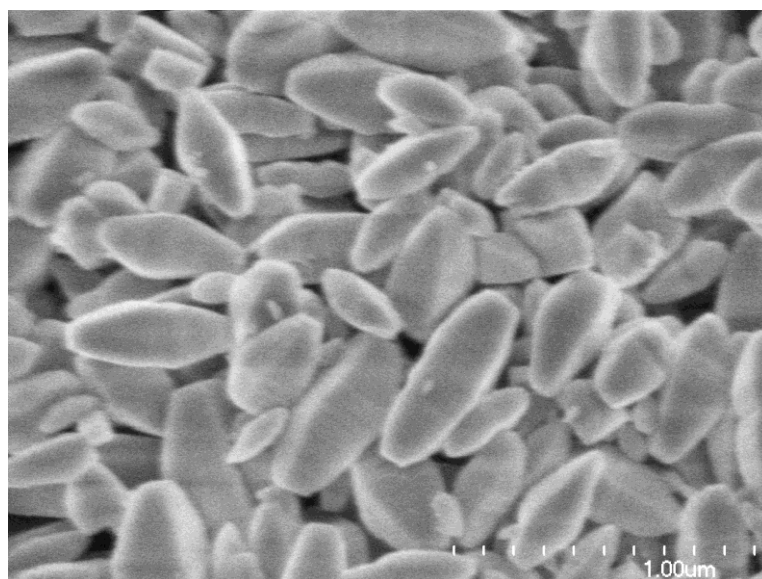


Figure 1.3: SEM image of ETS-10 crystals.

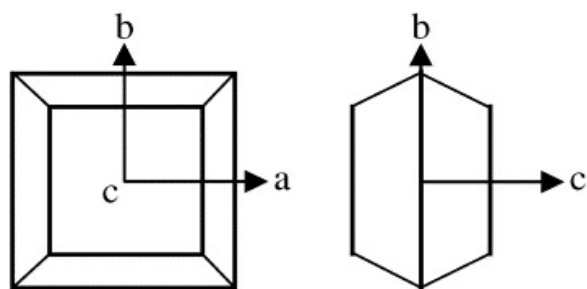


Figure 1.4: Schematic image of ETS-10 crystals [36].

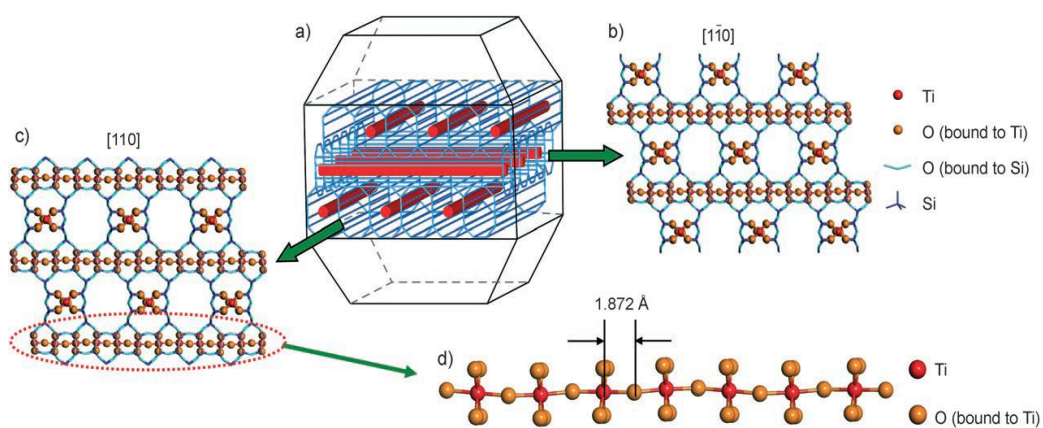


Figure 1.5: Crystal structure of polymorph B of ETS-10. a) Typical truncated-bipyramidal morphology of the crystals, which consist of a three dimensional network of SiO_2 channels (blue) and TiO_3^{2-} molecular wires (red). b) View along the $[\bar{1}10]$ axis. c) View along the $[110]$ axis. d) A single TiO_3^{2-} molecular wire [50].

1.2 Zeolite and Zeo-type Thin Films

For use in advanced and device-oriented applications, zeo-type and related molecular sieve crystals need to be supported on a substrate. Thus, preparation of thin films of these materials on various substrates have attracted considerable interest due to their potential use as molecular separation membranes, sensors, low-dielectric materials, and immobilized photocatalysts [2, 14–18].

Investigations on the attachment and/or formation of zeotype thin films on transparent conductive oxide (TCO) substrates, which is crucial for testing these materials for use in many advanced applications, are limited [4, 7, 8, 19–21]. TCO layers are widely used for the fabrication of different kinds of heterojunction solar cells. Indium tin oxide (ITO) is one of the most intensively studied TCO materials due to its high optical transparency, good electrical conductivity, low cost, excellent substrate adherence, high thermal stability, and chemical inertness [19, 22, 23]. Thus, the attachment and growth of zeo-type crystals on the ITO substrates might lead to a more extensive characterization and wider utilization of these materials in advanced applications [21].

Two methodologies have been used to prepare zeolite thin films on the ITO substrates. These methodologies are attaching the pre-synthesized zeolite crystals and growing the zeolite crystals on ITO substrates [19–21]. The attachment can be done either by transferring zeolite crystals onto ITO glass by microcontact printing [19] or using molecular linkers to attach uniformly sized microcrystals in the form of oriented zeolite monolayers [20]. The ITO glass-supported zeolite Y films with the average thickness of 2 μm were also prepared by the hydrothermal treatment of zeolite seed layers deposited by spin coating [21]. No information on the film orientation was provided. In general, the effective seeded (secondary)

growth of zeo-type films/membranes requires the use of appropriate growth mixture and synthesis conditions to substantially decouple nucleation from crystal growth, and to avoid/reduce the chemical attack of the support [24, 25]. However, the secondary growth technique might lead to thin films that are strongly bonded on the substrate, which is important for their end use in advanced applications [21].

1.3 Metal Nanoparticles

Nowadays, there are several literature reports related with preparation and characterization of nanostructured materials due to their unique properties and potential use in technological applications. When the shape and size of the nanoparticles are changed, their optical, magnetic, and electronic properties change significantly. The ultimate goal is to controllably alter the morphology and size of synthesized nanoparticles like metal and semiconductor nanoparticles.

1.3.1 Preparation Methods of Metal Nanoparticles

In order to prepare metallic nanoparticles there are several preparation techniques in the literature such as, reduction of the metal salt in solution by reducing agents such as sodium citrate, sodium borhydride or hydrogen [66], thermolysis [69], electrochemical synthesis [70,71], radiolytic techniques using γ -Ray source [67,68], photolysis [72], vapor flow condensation [73], electron beam lithography and nanotransfer printing [74-76]. Host materials such as, zeolites [77, 78],

micelles [84-86], and porous alumina [79-83] can be used in order to synthesize metal nanoparticles in preferred shape inside of these host materials.

Although there are various techniques dealing with preparation of metal nanoparticles, there are difficulties to synthesize metal nanoparticles in desired size with narrow distribution. Colloidal gold nanoparticles (~20 nm) have been synthesized by using reducing agent sodium citrate [66]. γ -Ray source can be used in radiolytic techniques in order to prepare silver (~3 nm) and gold (>1 nm) colloidal nanoparticles [68]. Other preparation methods are thermolysis [69], and photolysis [72] of unstable organometallic precursors that were used to synthesize palladium nanoparticles (10-100 nm) in organic solvents and colloidal platinum nanoparticles (1.4- 2.1 nm). Gold nanorods with aspect ratio 2.6-7.6 suspended in aqueous solutions [71], and palladium with diameter 4.8 nm [70] has been synthesized by using electrochemical synthesis methods. Bismuth metal nanoparticles (12-37 nm) have been synthesized by vapor condensation in tube flows [73].

As mentioned above, restricted environments such as polymer (~8 nm silver nanoparticles) [74-76] and micelles [84-86] (~ 2-10 nm copper nanoparticles) can be used in order to synthesize metal nanoparticles. Gold cylinders (aspect ratio 1.53-6.31) were prepared by electrodeposition technique within the pores of porous alumina membranes and alumina oxide membranes [79-83]. In the case of zeolites, there is no need to use stabilizers since they have suitable host structures which provides highly ordered cavities and channels. When zeolites are used as host materials in order to synthesize metal nanoparticles generally two-step procedure is used: first of all, metal cations are ion-exchanged with the extra framework cations of zeolites, then, ions are reduced by reducing agents such as sodium borohydride metal nanoparticles are created [77-78].

One of the most crucial problems in the preparation of metal nanoparticles is aggregation. They have tendency to convert into bulk metal, which is the thermodynamically most favorable state. In most of the methods, preparations have been made in an aqueous solution, using surfactants or polymers in order to stabilize the colloidal particles. When the reduction of the metal precursors was carried out in a restricted environment such as inside of zeolites or porous alumina, there was no need to use surfactants to stabilize metal nanoparticles. Colloidal nanoparticles have limited application areas since they are in liquid media. On the other hand, once the metal nanoparticles are reduced inside zeolite cages or channels, zeolite can be dried and can be used in the powder form without any agglomeration of metal nanoparticles formed inner or outer surface area of the zeolites. Furthermore, films of these metal nanoclusters including zeolite can be prepared on desired substrates such as glass, quartz or silicon by different attachment techniques. The preparation method is relatively cheap and easy when compared with vapor flow condensation and electron beam lithography preparation methods.

1.3.2 Surface Plasmon Resonance

The optical absorption spectra of the metal nanoparticles depend on their sizes. The distinct light absorption from metal nanoparticles is the collective oscillation of the conduction band electrons produced by an electromagnetic field [52]. These resonances are known as surface plasmons. The extinction coefficient of metal nanoparticles proportional with the volume of the particles can be larger than organic dye molecules [52]. The three factors for collective oscillations are acceleration of the conduction electrons by the electric field of incident radiation, presence of restoring forces that result from the induced polarization in both the

particle and surrounding medium, and confinement of the electrons to dimensions smaller than the wavelength of light [53-54]. The electrons of particles excited by the electric field of the EM radiation begin to oscillate with a characteristic frequency called surface plasmon resonance frequency. Dielectric constant of the surrounding medium affects the frequency of the surface plasmon resonance. Figure 1.6 shows the example of how the wavelength of the SPR can be shifted to the preferred position by changing the dielectric constant of the surrounding medium. In Figure 1.6-A, dielectric constant is decreased from isopropanol to Teflon AF, and the SPR is shifted to shorter wavelengths. In 1.6-B and 1.6-C the SPR wavelength is shifted to longer wavelengths by increasing the dielectric constant of the surrounding medium from water to silica and titania, respectively [53-54].

The dimensions of the particles have significant effect on the shape of the surface plasmon resonance spectrum since the size of the particles changes oscillation type of the conduction electrons [53-54]. For nanoparticles smaller than the wavelength of light (<20 nm) only dipole-type oscillation is observed in which all the conduction electrons move coherently (Figure 1.7-A). This oscillation type leads a single and narrow peak in the surface plasmon resonance spectrum.

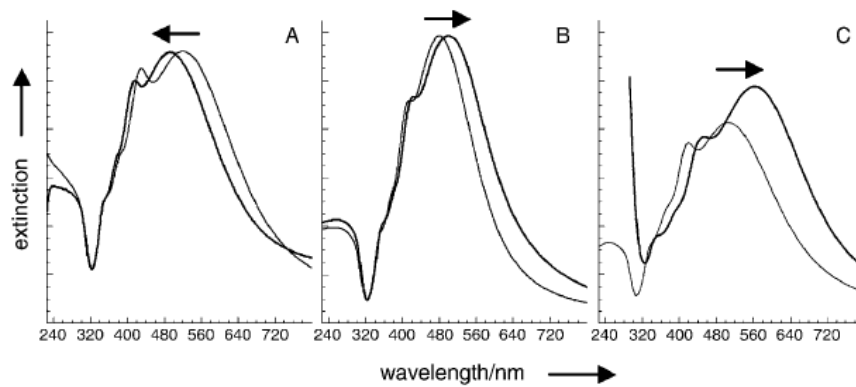


Figure 1.6: UV/Vis extinction spectra of silver nanoparticle suspensions before (c) and after (c) changes were made to the dielectric environment from A) isopropanol to Teflon AF, B) water to silica, and C) water to titania [53].

When the size increases, the EM field throughout the particle shows nonuniform property because of the phase retardation in EM field which causes broadening in the the dipole resonance. This leads multipole resonances, such as the quadrupole, octupole (Figures 1.7-B and 1.7-C). Thus, several peaks in the spectra are observed [53-54].

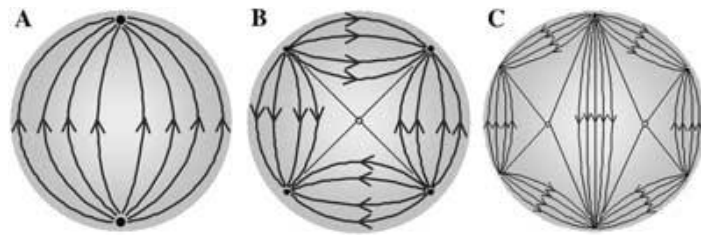


Figure 1.7: Diagrams depicting the electric field lines of the A) dipole, B) quadrupole, and C) octupole resonances, after ref. [53].

Some of the metals such as, copper, silver, and gold exhibits specific property since their plasmon resonance is strongest and shifted into the visible range. On the other hand, a broad absorption band is observed for the other transition metals in the ultraviolet region [52].

CHAPTER 2

LITERATURE SUMMARY

2.1 ETS-10 in Advanced Applications

ETS-10 with the ...O-Ti-O-Ti-O... chains which behaves as very thin quantum wire has band gap energy of ~ 4.03 eV [99]. For different types of reactions it is used as a catalyst [92,103,104]. It can be used to remove organic pollutants by using photocatalytic reactions [102] and harmful heavy-metal [101]. Corma et al. [4] tested activity of four different types of zeolites that contain titanium (Ti/Beta, Ti/Beta-60, TS-1 and ETS-10) for solar cell applications. The cells look like dye-synthesized solar cell after incorporation of N3 ruthenium dye exhibited open-circuit voltage $V_{OC} = 0.56$ V, short-circuit photocurrent density $I_{SC} = 0.1$ mA, and fill factor $FF = 0.34$. When compared P25 TiO_2 dye synthesized solar cell which has $V_{OC} = 0.77$ V, $I_{SC} = 4.22$ mA and $FF = 0.64$ [4], this results indicate that zeo-type materials could be used in dye synthesized solar cells.

ETS-10 is so unique material since it has periodically formed -O-Ti-O-Ti-O- quantum wires with a diameter of ~ 0.67 nm [100] which runs throughout the crystals in *a* and *b* directions. ETS-10 is a chemically inert large band-gap material containing a molecular wire. There is no other example for molecular wires or nanorods which are formed inside such kind of environment. Therefore, there

have been studies focusing on the length–band gap relationship of the titanate molecular wire. Zecchina et al. suggested that when the length of the TiO_3^{2-} wire inside the structure of the ETS-10 is longer than 25 nm the band gap does not depend on the length of the wire [99]. On the other hand, Yoon et al. showed that even if the length of the TiO_3^{2-} wire is longer than 50 nm it exhibits the quantum confinement effect throughout the direction of the wires [26]. It was suggested that [100] the predicted reduced mass of an exciton throughout its wire direction is μ_z , $0.0006m_e$ for ETS-10. This value is smaller than InSb ($0.014m_e$) and single-walled carbon nanotubes (SW-CNTs, $0.019m_e$) [100]. The unusually small μ_z suggests the possibility of greater carrier mobility throughout the TiO_3^{2-} molecular wire which could be attributed to the possibility of the fact that the quantum wire is metallic although the wire is in oxide form [100].

2.2 The Preparation of Zeolite and Zeo-type Thin Films

Literature on the supported ETS-10 thin film/membrane preparation is limited. Oriented films/membranes for use in molecular separations and photoluminescent devices were fabricated by hydrothermal treatment of ETS-10 or ETS-4 seed layers deposited/prepared on porous titania, α -alumina, and stainless steel supports [34–39]. Thin ETS-10 films for potential use in photocatalysis in the optical fiber reactors were also prepared by secondary growth of seed layers deposited on fused silica optical fiber surface modified by partially hydrolyzed tetraethyl orthosilicate [17]. Non-continuous films of ETS-10 crystals were assembled on 3-aminopropyltrimethoxysilane-functionalized n-type gallium nitride substrates [16]. These films were prepared for use in the potential photocatalytic applications without direct exposure of crystals to light, and to

more efficiently use photons available. To date, only one report described the preparation of ETS-10 films on a conductive transparent substrate for use in photovoltaic solar cells [4]. This film was prepared by spreading the ETS-10 crystals-containing α -terpineol-ethylcellulose paste on a fluoride-doped tin oxide (FTO) glass substrate using the doctor blade technique. The development of methods for the firm attachment of oriented ETS-10 crystals on the conductive transparent substrates is needed to further develop/open new areas for advanced application of ETS-10, such as photovoltaic and optoelectronics. In the present investigation, firmly bonded and oriented ETS-10 films were prepared on ITO glass substrates by applying the secondary growth technique.

2.3 The Application Areas of ETS-10 Containing Silver

Currently, there is not many literature work related directly with ETS-10 samples containing silver ion or nanoparticles. A few recent publications reported on various features of ETS-10 structure in this area [57, 93-95, 97, 98]. One of the main drawbacks in the extensive usage of ETS-10 in advanced applications such as in photocatalysis is its band gap value, which is located in the UV range and that does not allow the use of solar light [96]. In order to overcome this drawback, cation exchange capability of ETS-10 is widely used in many studies. Usually, ion exchanged ETS-10 can be prepared by the well known ion exchange procedures. ETS-10 containing nanoparticles can be produced by the reduction of these ion-exchanged samples. This can be done by several techniques, such as thermal-, chemical-, and UV-photo-treatments on Ag^+ -ETS-10 samples [94]. Upon producing the ETS-10 containing silver nanoparticles, it was shown that the light absorption of ETS-10 was shifted down to the visible region. This was shown as

an example to control the frequency of silver nanoparticle plasmon resonance and thus the light absorption properties of the obtained material.

Silver exchanged zeolites were also shown to exhibit unusual adsorption properties, toward the inert gases Ar, Kr and Xe [95]. Anson et al. studied the adsorption of argon, oxygen, and nitrogen on silver exchanged titanosilicate molecular sieve ETS-10 [97]. Modified ETS-10 was used in the strong adsorption of ethane and ethylene [93]. Tiscornia et al. characterized the silver ion exchanged ETS-10 samples by BET, XPS, and XRD, after which they investigated effect of Ag^+ content on adsorption properties of ETS-10 [57]. Another application area of ETS-10 containing silver nanoparticles was the use of these samples in bactericidal activities [98].

CHAPTER 3

EXPERIMENTAL

3.1 ETS-10 Synthesis

Titanosilicate ETS-10 crystals used in the seed layer formation step were hydrothermally synthesized using molar composition 3.4 Na₂O: 1.5 K₂O: TiO₂: 5.5 SiO₂: 150 H₂O [40]. In this preparation, sodium chloride and potassium chloride were dissolved in deionized water in a 60 mL high-density polyethylene (HDPE) bottle. After dissolving these components, sodium silicate was added and hand-shaken for 5 min, forming the Si precursor solution. For preparation of the Ti precursor solution, sulfuric acid was added to deionized water in another 60 mL HDPE bottle. P25 (Commercial TiO₂) was then added and hand-shaken for 5 min. After both precursor solutions were hand-mixed, the Ti precursor solution was poured into the Si precursor solution. The resulting mixture (white, viscous “gel”) was hand-shaken for 5 min. After measuring the pH (pH = 10.6–10.8) using an Orion pH meter model 720A, the mixture was transferred into 10 mL Teflon-lined stainless steel autoclaves. The static synthesis was carried out for 3 days at 503 K; the products were cooled to room temperature, filtered, washed with deionized water, and dried overnight in ambient air at ~343 K.

3.2 Preparation of ETS-10 Thin Films on Indium Tin Oxide Surfaces

In this study, a first time study was made in order to prepare firmly bonded and oriented ETS-10 films on ITO glass substrates by applying the secondary growth technique [105].

3.2.1 Methods

3.2.1.1 Secondary Growth

The film preparation procedure consisted of two steps: seed layer formation followed by growth of these seed crystals. In the first step, ETS-10 seed crystals were deposited by dip coating the ITO glass substrates. The ITO glass (Nanocs, purity 99%, resistivity 10 Ω /sq) substrates (\sim 7mm x \sim 25 mm) were cleaned by successive ultrasonication in acetone, ethanol, and 2-propanol, each sonication step carried out for 20 min, followed by 20-min drying in ambient air at 353 K. The pre-cleaned substrates were then immersed for 20 s in an ethanol suspension containing 5 wt. % of submicrometer-sized ETS-10 crystals. These crystals were synthesized hydrothermally using modified procedure of Lv et al. [40] (Section 3.1). After removing from the dip coating suspension, the substrates were immediately air-dried using an air gun, and then left for \sim 30 min to dry at room

temperature in ambient air. Multiple dip coating steps were accomplished by repeating the substrate immersion and air drying procedure outlined above. The seeded substrates were heat-treated in ambient air (heating from 303 K to 773 K at 5 K/min, isothermal heating at 773 K for 540 min, and convective cooling to 303 K). In the second step of ETS-10 film preparation, the seed crystals deposited on ITO glass substrates were grown using the modified procedure of Ji et al. [17]. In this secondary growth step, the ITO glass substrates with seed layers facing downwards were diagonally placed in the Teflon-lined 10 mL stainless steel autoclaves (Figure 3.1).

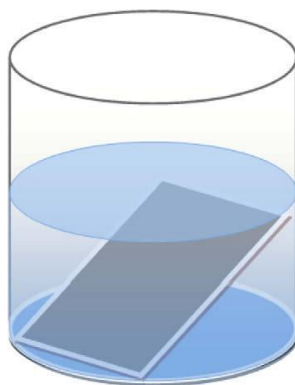


Figure 3.1: Schematic illustrating the orientation of the ITO glass substrates in the autoclaves used in the secondary growth step.

Then, the autoclaves were carefully filled with secondary growth mixture (mixture preparation procedure is described elsewhere [41]). The substrates were completely submerged in the growth mixture. After a 4-h static hydrothermal

treatment at 473 K, the contents of the autoclaves were cooled to room temperature in cold water. Some phase separation/settling in the growth mixture was observed after hydrothermal treatment; however, the white colored fluid still covered the substrates. The ETS-10 films supported on the ITO glass substrates were removed from the growth mixture, thoroughly rinsed with deionized water, immediately air-dried using an air gun, and left overnight to dry at room temperature in ambient air.

3.3 Preparation of ETS-10 Containing Silver Nanoparticles

ETS-10 containing Ag⁰ nanoparticles was prepared by two-step procedure: first of all, extra framework Na⁺ and K⁺ ions in ETS-10 exchanged with Ag⁺ ions by using different AgNO₃ concentrations, then, ions reduced to silver metal nanoparticles. In order to reduce Ag⁺ to Ag⁰ sodium borohydride in aqueous solution was used at room temperature.

3.3.1 Methods

3.3.1.1 Ag⁺ Ion-exchange and Reduction of Ag⁺ Ions

The ion-exchange was used in order to obtain Ag⁺-exchanged ETS-10 samples: 500 mg of as-synthesized ETS-10 crystals were added to a 100 mL aqueous AgNO₃ solution with different molar concentration (4.12 mM, 0.5 M). The

solution was stirred vigorously for 24h. After ion exchange, the samples were washed several times by centrifugations. ETS-10 containing silver nanoparticles preparation was carried out by reducing Ag^+ -exchanged ETS-10 in sodium borohydride suspension at room temperature. H_2 outflow were observed by naked eye after addition of sodium borohydride when it finished the samples were filtered, washed with 1 L of deionized water. The samples dried overnight at 100 °C.

3.4 Material Characterization

3.4.1 X-Ray Diffraction (XRD)

The X-ray powder diffraction (XRD) analysis of ETS-10 thin films were carried out using $\text{Cu K}\alpha$ radiation (40 kV, 30 mA) on a Bruker D5005 θ :2 θ Bragg-Brentano diffractometer equipped with a curved graphite crystal diffracted beam monochromator and a NaI scintillation detector. The degree of out-of-plane preferred orientation of ETS-10 crystals in seed layers/films was quantified by comparing the integrated intensities (i.e., areas) of selected ETS-10 peaks in the XRD patterns of the seed layers/films and the powder sample. The integrated intensity and full-width-at-half-maximum (FWHM) of XRD peaks were determined using the Bruker Profile software. Phase identification of the synthesized ETS-10, ion-exchanged ETS-10 and ETS-10 containing silver nanoparticles were done by powder X-Ray diffraction analysis (XRD) using Ni filtered $\text{Cu-K}\alpha$ radiation (Philips PW 1729). The voltage and current were 40 kV /

30 mA, respectively. The diffraction peaks were scanned between 5-40° 2θ degrees with step size of 0.03° and 0.1°/s. Time constant was 1s, and slit was 0.2 mm.

3.4.2 Scanning Electron Microscopy (SEM)

The field emission scanning electron microscope (FE-SEM) images of ETS-10 thin films were acquired for uncoated samples using a Hitachi S-4700 FESEM (accelerating voltage 2 kV, beam current 10 μA) in the secondary electron imaging mode. The film cross-sections were imaged on the broken edges after breaking the film-containing ITO glass substrates. The Si/Ti ratios for seed crystals in a powder form and for columnar grains in the film cross-sections were measured using energy dispersive X-ray spectroscopy (EDX) utilizing a Phoenix EDAX X-ray analyzer equipped with Sapphire super ultra thin window detector attached to the Hitachi S-4700 FE-SEM (accelerating voltage 12 kV, beam current 10 μA). Morphological properties of the Ag⁺ loaded ETS-10 and as well as Ag⁰-ETS-10 were examined by scanning electron microscopy (SEM) (FEI Quanta 400).

3.4.3 Inductively Coupled Plasma - Optical Emission Spectrometry (ICP-OES)

Silver content of the ion-exchanged and ETS-10 containing silver nanoparticle were determined by inductively coupled optical emission spectrometry (ICP-OES,

Perkin Elmer Optima 4300DV) after total dissolution of the ETS-10 samples by microwave digestion.

3.4.4 UV-VIS Spectroscopy

The UV-visible spectra in diffuse reflectance mode were recorded on a Shimadzu (UV-2450) UV-VIS spectrophotometer, from 200 to 800 nm. Spectrums were recorded in the powder form by squeezing a small amount of powder in a holder. Diffuse reflectance spectra were converted to absorption spectra by applying Kubelka-Munk Function [117]. In the Kubelka-Munk Theory two fluxes I and J are incident and scattered light flux, respectively. They are perpendicular to the surface of the powdered sample. As explained in the theory when the sample is relatively thick, the diffuse reflection of the sample (R) is related to an absorption (K) and scattering (S) coefficient as follows:

$$F(R) = \frac{(1-R)^2}{2R} = \frac{K}{S} \quad (3.1)$$

3.4.5 X-Ray Photoelectron Spectroscopy (XPS)

To investigate bonding of the metal Ag nanoparticles, X-ray photoelectron spectroscopy (XPS) analysis were performed. The XPS analysis was carried out

on a Physical Electronics 5800 spectrometer. Radiation source was Mg 244 W. The binding energies were referenced to the internal standard C 1s (284.9 eV).

3.4.6 Surface and Pore Size Analysis

To investigate the difference of pore openings and surface areas after silver incorporation surface and pore size analysis were carried out. The nitrogen adsorption/desorption experiments were carried out at by NOVA 3000 series (Quantachrome Instruments) instrument. Sample preparation method includes outgassing samples under vacuum at 573 K for 3 h before analysis.

3.4.7 Transmission Electron Microscopy (TEM)

To observe framework stability and silver nanoparticle formation transmission electron microscopy images were taken. For TEM imaging JEM-2010F microscope (JEOL) was used. Operating voltage was 200 kV. One drop of ETS-10 suspended in ethanol was placed on the copper grid of the transmission electron microscope.

3.4.8 Transmittance-Reflectance Measurements

ETS-10 and Ag⁰-ETS-10 on ITO glass and quartz substrates were prepared by 3 times dip-coating for measurements. Powder ETS-10 and Ag⁰-ETS-10 were dispersed in ethanol (5 wt. %) and sonicated for 45 minutes. ITO glass and quartz substrates were dip-coated with the suspension for 3 times. In each step substrates were dried in 90 °C oven for 10 minutes. Transmittance-Reflectance measurements were carried out by an optical microscope. The optical microscope (Leitz) with both reflection and transmission mode was coupled to a monochromator through a multimode fiber.

CHAPTER 4

RESULTS AND DISCUSSION

4.1 Synthesis of ETS-10

The first step was to investigate the optimum synthesis conditions and identify the most appropriate titanium and silica precursor in order to obtain pure ETS-10 crystals and growth of ETS-10 film. For these purposes, the effect of titanium and silica sources that had been and have not been studied by others, pH of synthesis gel, molar compositions, synthesis time and temperature on the crystallization and growth of ETS-10 were reported. Three optimized gel synthesis systems, i.e., 3.4 Na₂O: 1.5 K₂O: TiO₂: 5.5 SiO₂: 180 H₂O (System I) [40], 3.4 Na₂O: 1.5K₂O: TiO₂: 5.5 SiO₂: 150 H₂O (System II) [40], and 4.55 Na₂O: 1.5 KF: TiO₂: 5.5 SiO₂: 300 H₂O (System III) [17] were used to examine the synthesis conditions for both halfmicron-sized ETS-10 synthesis and secondary growth solutions. In order to investigate the effect of temperature and pH values to form pure crystal of ETS-10 and growth of film in the optimized systems synthesis temperatures of 200 and 230 °C were used between the pH range of 10.3 - 11.7.

4.1.1 Effect of Composition and Source Materials

There is a small number of reports on the synthesis of halfmicron-sized ETS-10. Liu and Thomas [90] reported that under correct synthetic conditions, nano-sized Degussa TiO₂ (P25) can be used as a Ti source to prepare pure ETS-10. Rocha et al. [91] showed that ETS-10 can be synthesized by using a pure anatase phase of TiO₂. Yoon et. al. reported 0.3 μm-sized ETS-10 by using titanium isopropoxide as a titanium source. In this study, halfmicron-sized ETS-10 crystals were synthesized with both P25 and TiO₂ (mixture of anatase and rutile). These crystals were synthesized hydrothermally using modified procedure of Lv et al. [40]. From each titanium source, pure crystals were obtained at proper crystallization temperature and time. It was observed that when the crystallization time was increased, intergrown crystals and rutile impurity were formed.

Ti₂(SO₄)₃ (TS-992) from Kerr McGee Corp. was used as the Ti source in the previous report of ETS-10 film preparation [17]. Oriented polycrystalline ETS-10 thin films (average thickness ~1.50–1.75 μm) on the ITO glass substrates were obtained in the current study using the modified procedure of Ji et al. [17]. However, Kerr McGee Corp. stopped the production of Ti₂(SO₄)₃ (TS-992). Thus, alternative Ti sources for secondary growth solution have been widely searched. Instead of using Ti₂(SO₄)₃ (TS-992), Ti₂(SO₄)₃ from Aldrich and TiCl₃ from Fisher were employed. (i) Through using TS-992 as a Ti source with molar composition which is given in the literature [17] pure micron-sized ETS-10 (=secondary growth mixture) and oriented ETS-10 films were obtained after 2 days of hydrothermal synthesis after 4 hours, respectively. (ii) When TiCl₃ was used as a Ti source with System I, even though pure micron-sized ETS-10 (=secondary growth mixture) could not be obtained after 3, 4 and 7 days, ETS-10 films were obtained with this mixture after 6 hours. (iii) Through using Ti₂(SO₄)₃ from Aldrich as a Ti source with System I and III, pure micron-sized ETS-10

(=secondary growth mixture) could not be obtained. However, ETS-10 films were obtained successfully by using this mixture as a secondary growth solution after 6 hours. Although, pure micron-sized ETS-10 were not obtained after hydrothermal synthesis upon using TiCl_3 from Fisher and $\text{Ti}_2(\text{SO}_4)_3$ from Aldrich as a Ti source, oriented ETS-10 films were obtained successfully through using these mixture as a secondary growth solution .

4.1.2 Effect of Synthesis Conditions

The pH of an initial synthesis gel is important for zeolite crystallization since OH^- pretend to be a mineralizing agent. Therefore, pH of the gel is believed to adjust the degree of polymerization of silicate species in synthesis gel [40]. In the current study, the desired pH values in System I-II-III controlled by using H_2SO_4 or NaOH solutions. In the synthesis gel of halfmicron-sized ETS-10 and growth solution of ETS-10 film using all different Ti sources and silica sources, the pH range of the synthesis gel was kept between 10.3-11.7.

Another important factor for synthesis is the temperature. The crystallization temperature affects the solubility of sources; thus, the formation of nuclei in the synthesis gel. Therefore, crystallization temperature is crucial for the formation of pure crystals. In the present study, in order to investigate temperature effect on the synthesis condition, two different crystallization temperatures were used, which were 200 and 230 °C.

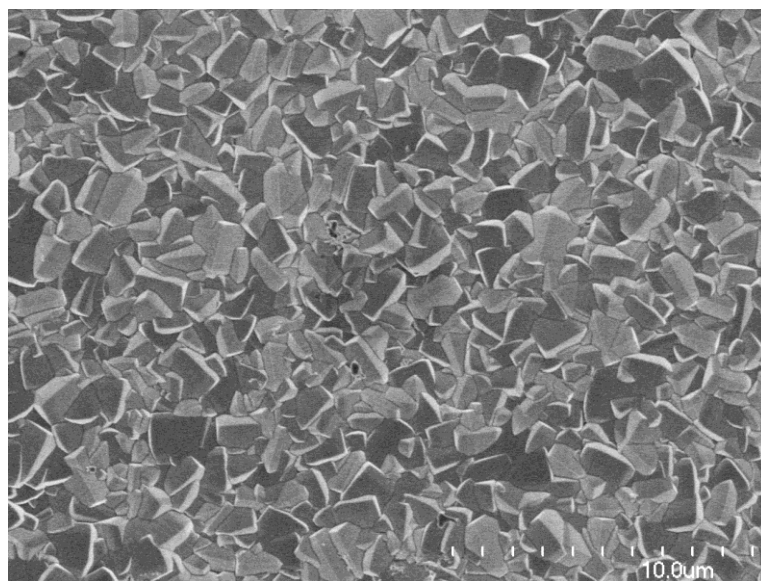


Figure 4.1: SEM image of secondary growth of ETS-10 using System I.

The ETS-10 film obtained by secondary growth methodology using system I is shown in Figure 4.1. XRD patterns of secondary growth mixture gel and film are given in Figure 4.2 and Figure 4.3, respectively. ETS-10 structure was expected from each XRD pattern. Both of them showed ETS-10 structure. However, secondary growth mixture showed ETS-10 structure with peaks coming from unreacted gel and quartz impurity, as well. Although there were large quantities of quartz impurity in the secondary growth mixture (Figure 4.2 red square), there was no quartz formation in the film obtained from the same secondary growth mixture as observed from the XRD analysis (Figure 4.3). It is possible that, during the secondary growth there was not enough time to form quartz on the obtained film.

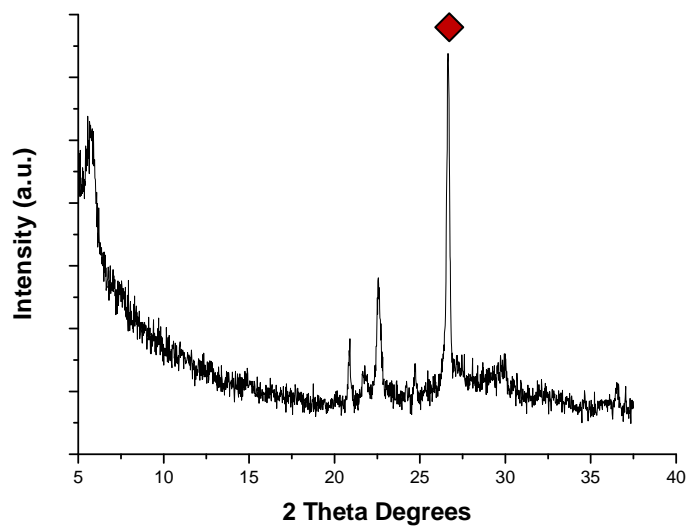


Figure 4.2: XRD pattern of hydrothermal synthesis of micron-sized ETS-10 using System I. Quartz impurity (red square).

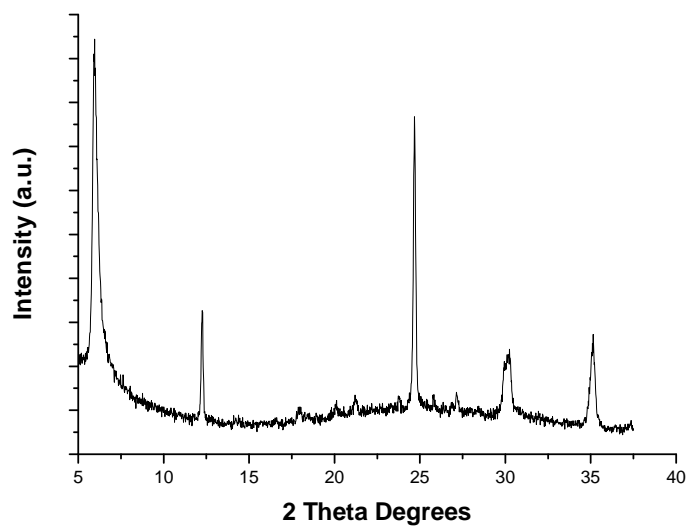


Figure 4.3: XRD pattern of ETS-10 film using System I as a secondary growth solution.

Table 4.1 shows micron-sized ETS-10 synthesis and secondary growth film trials with different Ti sources. It is obvious that, Ti sources have significant effect on obtaining pure micron-sized ETS-10 (=secondary growth mixture) and oriented film. Pure micron-sized ETS-10 were obtained by using TS-992 while impurities were obtained by using $Ti_2(SO_4)_3$ from Aldrich and $TiCl_3$ from Fisher. Upon using titanium sulfate sources more a(b)-out-of-plane oriented films were obtained. As a result, Ti sources and synthesis conditions were observed to effect ETS-10 products significantly.

Table 4.1: Summary of ETS-10 synthesis and ETS-10 films trials.

Purpose	Molar Comp.^a	Titanium Source Materials	Time	Temp. (C°)	pH	Results^b
Halfmicron-sized ETS-10	System II	P25	3, 4 days	230	10.6 -10.8	Pure ETS-10 crystals
Halfmicron-sized ETS-10	System II	TiO ₂ (mixture of anatase and rutile)	3, 4, 5 days	200 - 230	11.4 -11.7	Pure ETS-10 crystals
Micron-size ETS-10	System III	TS-992	2 days	200	10.8	Pure ETS-10 crystals
Secondary Growth of ETS-10 Film	System III	TS-992	4 hours	200	10.8	SG of ETS-10 film
Micron-sized ETS-10	System I	Ti ₂ (SO ₄) ₃ from Aldrich	3, 5, 7 days	230	10.4 -10.8	ETS-10 crystals + impurity
Secondary Growth of ETS-10 Film	System I	Ti ₂ (SO ₄) ₃ from Aldrich	6, 8, 10 hours, and 1 day	230	10.6 -10.8	SG of ETS-10 film
Micron-sized ETS-10	System I	TiCl ₃ from Fisher	4, 5, 7 days	230	10.3 -10.6	ETS-10 crystals + impurity
Secondary Growth of ETS-10 Film	System I	TiCl ₃ from Fisher	6, 8, 10 hours, and 1 day	230	10.3 -10.4	SG of ETS-10 film

^a3.4 Na₂O: 1.5K₂O: TiO₂:5.5 SiO₂:180 H₂O (System I), 3.4 Na₂O: 1.5K₂O: TiO₂:5.5 SiO₂:150 H₂O (System II), and 4.55 Na₂O:1.5 KF: TiO₂:5.5 SiO₂:300 H₂O (System III)

^bSG: Secondary growth of ETS-10 film

4.2 Preparation of ETS-10 Thin Films on Indium Tin Oxide Surfaces

4.2.1 Methods

4.2.1.1 Seed Layer Formation

Figure 4.4 shows the top view FE-SEM image of an ETS-10 seed layer deposited on the ITO glass substrate using a single dip coating step. As shown in Figure 4.4 and its inset, the seeds were closely packed forming an apparently continuous layer, although there were intercrystalline gaps present on the outer surface of this seed layer. FE-SEM analysis suggested a considerable a(b)-out-of-plane preferred orientation of crystals on the outer surface of the seed layer prepared using a single dip coating (Figure 4.4).

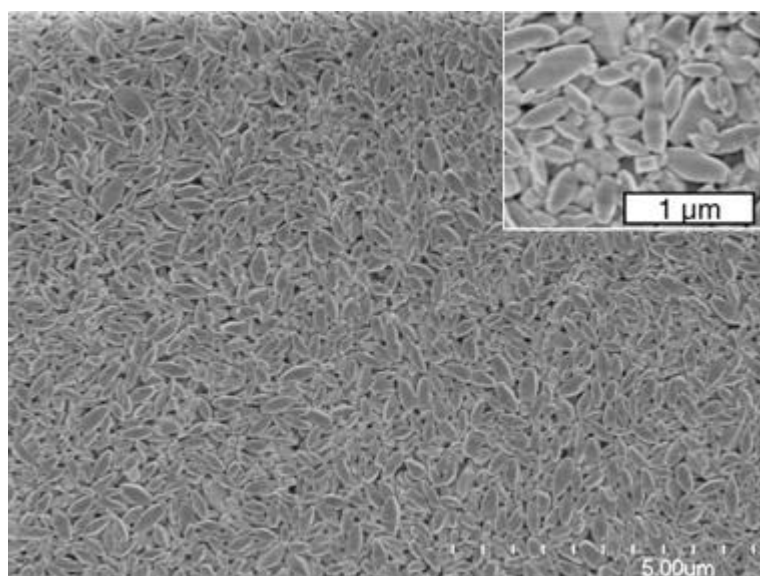


Figure 4.4: Top view FE-SEM image of the seed layer deposited using a single dip coating step.

This crystal orientation can be expected from the highly anisotropic shape of the ETS-10 seeds that causes the crystals to assemble in such a way that their larger pyramidal side surfaces, which contain crystals in a and b directions [43], adhere to the substrate surface.

Similar crystallographic texture was observed on the outer surfaces of seed layers deposited using 2 and 3 dip coating steps (Figure 4.5, 4.6). These seed layers also appeared to be continuous over a large (i.e., centimeter scale) area, although, similar to the single dip-coated seed layer, the intercrystalline gaps were observed on the outer surfaces. Even though complete randomness cannot be ascertained using this technique, FE-SEM observations suggested that the crystals at the top surfaces in all seed layers had rather random in-plane orientations relative to rotations about axes normal to the plane of the ITO glass substrate (Figure 4.4-4.6).

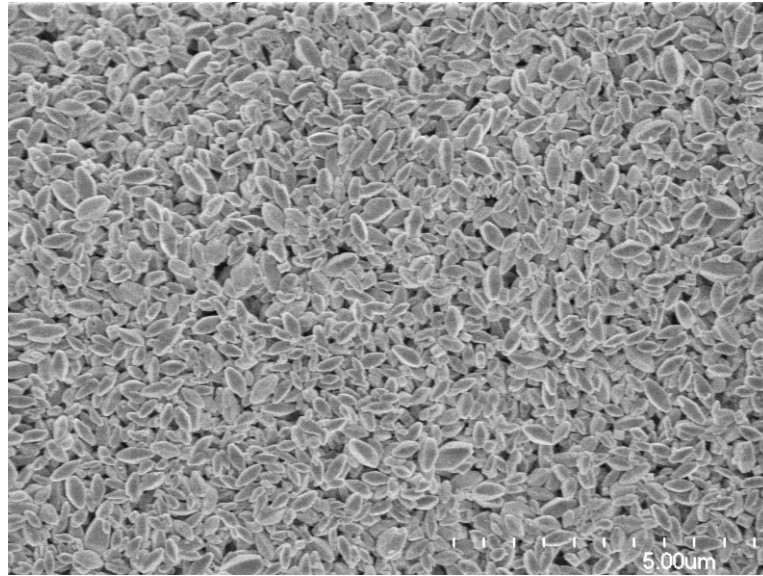


Figure 4.5: Top view FE-SEM image of the seed layer deposited using a double dip coating step.

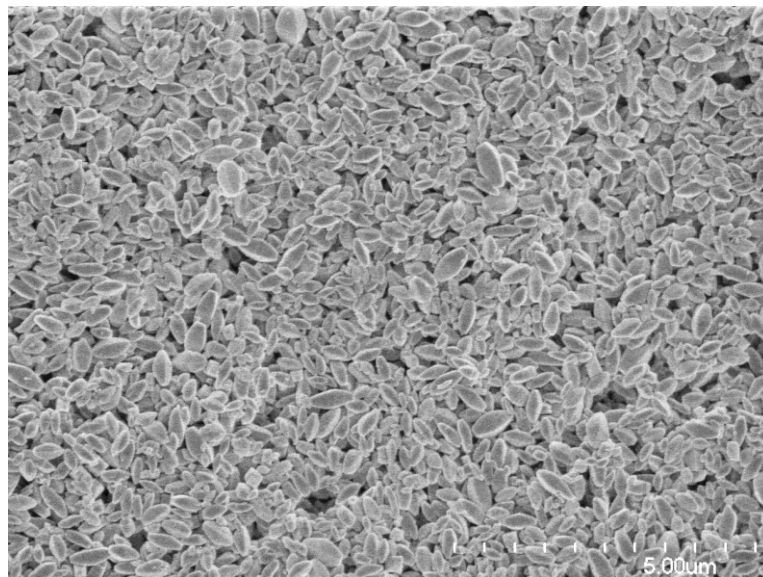


Figure 4.6: Top view FE-SEM image of the seed layer deposited using a triple dip coating step.

4.2.1.2 Secondary Growth

Instead of depositing the pre-synthesized ETS-10 crystals on ITO substrates, growing conditions of these crystals were investigated to improve the films and to obtain a strongly held ETS-10 layer on the substrates. In the literature, secondary growth technique using nano ETS-10 crystals as seed layers previous to the growth step is a widely studied methodology for such zeolite film growth purposes. In the present study, growing an ETS-10 thin film on ITO substrates with and without seeding was undertaken.

Figure 4.7 shows the morphology of ETS-10 crystals synthesized in the absence of seeds using the secondary growth mixture in 2-day crystallization. These crystals had also a truncated tetragonal bipyramidal habit typical for ETS-10 growing via a two-dimensional nucleation mechanism [46], but were more equiaxed than the seed crystals (Figure 4.4). The morphological variation shown in Figure 4.4, 4.5, 4.6, and 4.7 results from the change in the degree of development of the square (i.e., c direction) and trapezoidal (a and b directions) ETS-10 crystal facets [46], and can be attributed to the variation of the relative normal growth rates of these facets. Since the face with the lowest normal growth rate is the largest in the crystal (i.e., sizes of crystal faces are inversely related to their normal growth rates), the ratio of the crystal growth rate in the a and b directions to that in the c direction was higher during the crystallization in the secondary growth mixture than in the gel used to synthesize the seed crystals. Thus, the conditions at the early stages employed in the secondary growth step may have resulted in a faster growth of the seed crystals along their a and b directions. This would lead to the self-orienting film development as inferred from the quantitative XRD results ($\text{CPO}_{(200)/(105)}$ values were for 2-seed layer = 13 ± 3 , 3-seed layer = 9 ± 4 , 1-Film = 31 ± 2 , 2-Film = 28 ± 3 , 3-Film = 15 ± 4 as listed in Table 4.2).

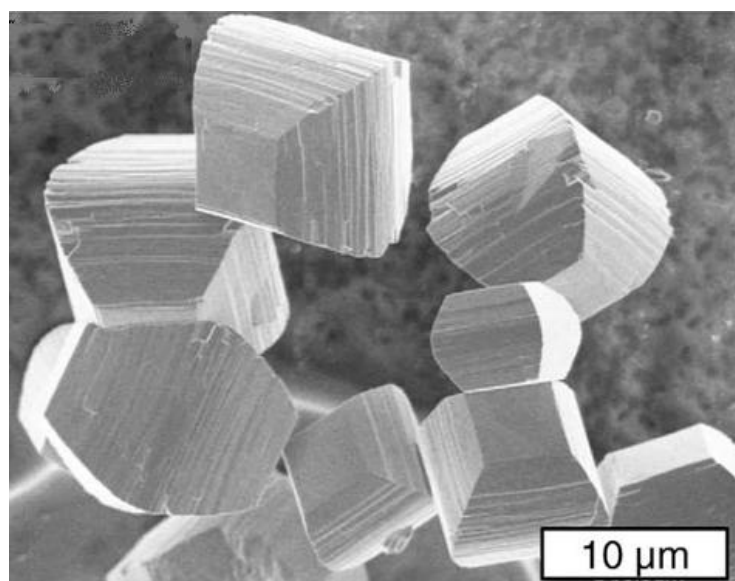


Figure 4.7: FE-SEM image of crystals synthesized in a 2-day unseeded hydrothermal crystallization using the secondary growth mixture.

4.2.2 Microstructural Characterization of ETS-10 Thin Films

Microstructural characterization of oriented titanosilicate ETS-10 thin films was carried out by XRD and SEM.

4.2.2.1 Ti-O-Ti-O-Ti- Wire Orientation and XRD Analysis

XRD pattern of the powder sample of seed crystals recovered from the ethanolic dip coating suspension showed a phase-pure ETS-10 product (Figure 4.8 b). This pattern was identical to the XRD patterns of as-synthesized as well as calcined at 773 K ETS-10 seed crystals (not shown). As shown in Figure 4.4, the seed crystals were in the form of elongated square-based truncated bipyramids, which did not exceed $\sim 1.0 \mu\text{m}$ in length (c direction) and $\sim 0.5 \mu\text{m}$ in width (a and b directions). Suspending the seeds in ethanol and calcination at 773 K affected neither crystal morphology/topography as determined by FE-SEM nor product crystallinity as determined from the FWHM of 202 ETS-10 reflection at $\sim 24.7^\circ 2\theta$ (the indexing of ETS-10 reflections is based on the superposition model of Wang and Jacobson [42]).

XRD analysis (Figure 4.8 c–e) suggested that applying more dip coating steps resulted in an increase in the thickness of the seed layers. This was deduced from the gradually increasing intensity of 202 ETS-10 reflection at $\sim 24.7^\circ 2\theta$ relative to the ITO peak at $\sim 35.2^\circ 2\theta$. The patterns in Figure 4.8 c–e also qualitatively confirmed the crystallographic texture of the deposited seed layers obtained from FE-SEM observations. Owing to the preferred crystal orientation effects in the seed layers, the relative intensities of the specific reflections in the XRD patterns of these layers (Figure 4.8 c–e) and the (randomly oriented) ETS-10 powder sample (Figure 4.8b) were different. Specifically, the relative intensities of (105), (116), and (204) reflections significantly decreased, whereas the relative intensity of (200) reflection slightly increased for the seed layers compared to the powder sample. This indicates a(b)-out-of-plane preferred ETS-10 crystal orientation [34–36] in the seed layers. Also, in agreement with similar observations for ETS-10 membranes with the same crystallographic texture [35], the peak at $\sim 6^\circ 2\theta$ was relatively sharper/more intense in the XRD patterns of seed layers than the powder sample (Figure 4.8).

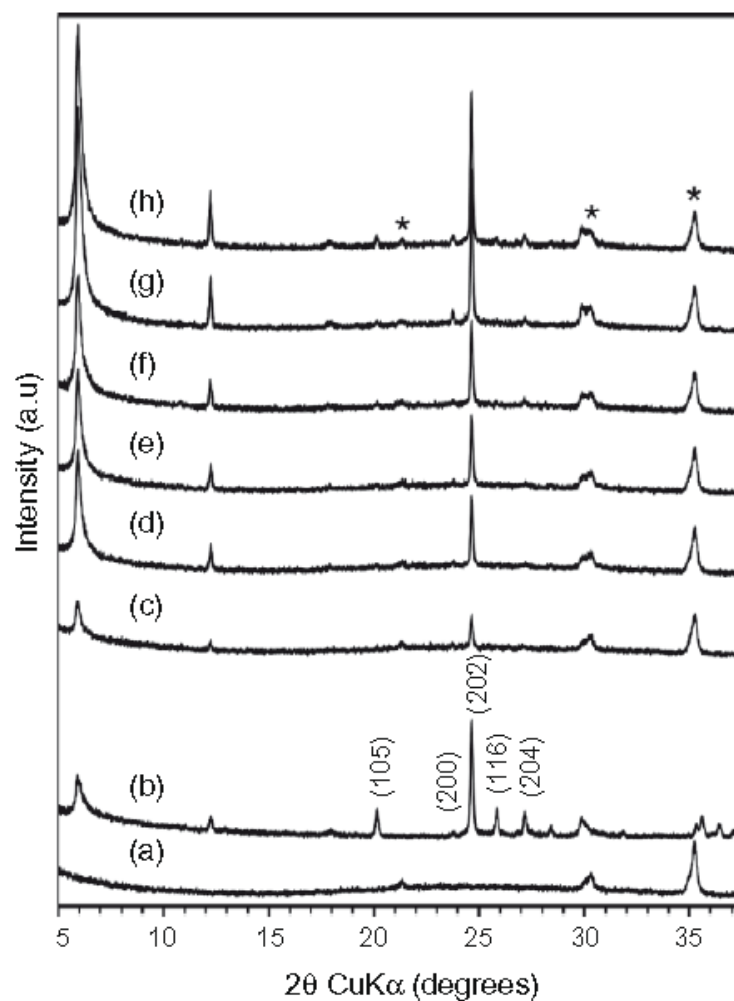


Figure 4.8: XRD patterns of bare ITO glass substrate (a), ETS-10 powder (b), seed layers deposited on the ITO glass substrate using 1 (c), 2 (d), and 3 (e) dip coating steps, and films after secondary growth of seed layers deposited via single (f), double (g), and triple (h) dip coating. The star symbols depict the reflections of the ITO substrate in the patterns of ETS-10 seed layers and films.

Quantitative assessment of the degree of a(b)-out-of-plane preferred crystal orientation in seed layers was performed by calculating the crystallographic preferred orientation (CPO) index based on (200) and (105) reflections. This index is defined as,

$$\text{CPO}_{(200)/(105)} = \{ (I_{(200)}/I_{(105)})_f - (I_{(200)}/I_{(105)})_p \} / (I_{(200)}/I_{(105)})_p \quad (4.1)$$

where, I is the integrated intensity of the corresponding reflections, and the superscripts f and p refer to the preferentially oriented sample and the randomly oriented (i.e., powder) sample, respectively [34–36]. The $\text{CPO}_{(200)/(105)}$ values calculated for seed layers obtained using 2 and 3 dip coating steps are shown in Table 4.2. The $\text{CPO}_{(200)/(105)}$ index could not be calculated for the single dip-coated seed layer because of the very weak (105) and (200) peaks, and the associated high uncertainty in the integrated intensity values for these peaks. As shown in Table 4.2 by decreasing the $\text{CPO}_{(200)/(105)}$ values, the degree of a(b)-out-of-plane preferred crystal orientation in the ETS-10 seed layers appeared to decrease with increasing number of dip coating steps, but it was substantial as defined from the comparison with the literature [34–36]. The decreasing degree of a(b)-out of-plane preferred crystal orientation in seed layers deposited by applying more dip coating steps is consistent with other literature observations for ETS-10 crystals with a similar morphological anisotropy [17].

Cross-sectional analysis revealed that the overall film (i.e., seed layer and columnar grains) thickness depended on the seed layer used in the secondary growth step, and increased from $1.50 \pm 0.15 \mu\text{m}$ to $1.75 \pm 0.25 \mu\text{m}$ (Table 4.2) when the number of dip coating steps employed to deposit seed layers increased from 1 to 3. However, the thickness of the columnar grains measured in the plane normal to the substrate surface was constant ($1.00 \pm 0.10 \mu\text{m}$), regardless of the seed layer used in the secondary growth step (Table 4.2). This is consistent with

the fact that in all cases the same growth mixture and duration of hydrothermal treatment were used during the secondary growth step, and suggests that film development occurred by epitaxial growth of crystals on the top surfaces of the seed layers. XRD analysis revealed the larger intensities of (202) ETS-10 reflection at $\sim 24.7^\circ 2\theta$ relative to the intensity of ITO peak at $\sim 35.2^\circ 2\theta$ for the films (Figures 4.8 f–h) than for the corresponding seed layers (Figures 4.8 c–e). This is consistent with the cross-sectional analysis results described above (i.e., larger thickness of films than the seed layers, Table 4.2). As for seed layers, the XRD patterns suggested the significant a(b)-out-of-plane preferred crystal orientation in final films (Figure 4.8 f–h). This was inferred from a strong decrease of the relative intensities for (105), (116), and (204) reflections, and a marked increase of the relative intensity for 200 reflection in the films (Figures 4.8 f–h) compared to the ETS-10 powder sample (Figure 4.8 b). Since the main channels and quantum wires run along ETS-10 crystal *a* and *b* directions [32, 43], this orientation should facilitate (mass, electrical) transport across the films. The $CPO_{(200)/(105)}$ values calculated for films grown from seed layers deposited using 1, 2 and 3 dip coating steps are shown in Table 4.2. As for the seed layers deposited using more dip coating steps, the decreasing $CPO_{(200)/(105)}$ values for films (i.e., seed layers and columnar grains) prepared from these seed layers indicated a decreasing degree of preferential crystal orientation with the increasing number of dip coating steps. However, the degree of a(b)-out-of-plane orientation was higher in films than in the corresponding seed layers, as indicated by their respective $CPO_{(200)/(105)}$ values (Table 4.2). These results indicate an effective self-alignment of the seed crystals during the secondary growth step, and may be attributed [25,45] to the faster growth of seeds along their *a* and *b* directions, and the competitive crystal growth in a confined growth space provided by the close packing and crystallographic orientation distribution of crystals in the seed layers.

Table 4.2: Seed layer thickness, film thickness, columnar grains thickness, and crystallographic preferred orientation index $CPO_{(200)/(105)}$ for ETS-10 films prepared via secondary growth of ETS-10 seed layers deposited using 1, 2, and 3 dip coating steps.

No. of dip coating steps	$CPO_{(200)/(105)}^a$	Thickness (μm)	Thickness of columnar grains (μm)
1 – Seed layer only	N/A ^b	0.50 ± 0.15	N/A
2 – Seed layer only	13 ± 3	0.60 ± 0.20	N/A
3 – Seed layer only	9 ± 4	0.75 ± 0.25	N/A
1 – Film^c	31 ± 2	1.50 ± 0.15	1.00 ± 0.10
2 – Film^c	28 ± 3	1.60 ± 0.20	1.00 ± 0.10
3 – Film^c	15 ± 4	1.75 ± 0.25	1.00 ± 0.10

^a $CPO_{(200)/(105)} = \{ (I_{(200)}/I_{(105)})_f - (I_{(200)}/I_{(105)})_p \} / (I_{(200)}/I_{(105)})_p$, where $I_{(200)}$ and $I_{(105)}$ is the integrated intensity of (200) and (105) ETS-10 reflections, respectively; and the superscripts f and p refer to the preferentially oriented sample and the powder sample, respectively [35–37].

^b Could not be calculated.

^c Film = seed layer + columnar grains.

4.2.2.2 Morphology of ETS-10 Thin Films

Figure 4.9 shows typical top view and cross-section FE-SEM images of ETS-10 films prepared by secondary growth of seed layers deposited using different number of dip coating steps. As illustrated in Figures 4.9 a, c and e, these polycrystalline films appeared to be continuous, i.e., the intercrystalline gaps observed on the top surfaces of seed layers (Figure 4.4) were absent on the top film surfaces. Evidently, the secondary growth step led to the seed crystal impingement, resulting in the formation of grain boundaries in the film. The size of the grains at the top film surfaces measured in the plane parallel to the substrate

(in-plane grain sizes) increased compared to the in-plane sizes of seed crystals (Figures 4.9 a, c, e, and Figure 4.4). Film cross-sections (Figures 4.9 b, d and f) showed columnar grains in the upper film portions, and the discernible crystal layers in the lower portions of the film. This completely different microstructural characteristics of films in their lower and upper parts indicated that the films evolved from seed layers by grain growth during the secondary growth step. In all cases, the seed layers were composed of crystal multilayers (Figures 4.9 b, d and f). Also, increasing number of dip coating steps from 1 to 3 appeared to increase thickness and decrease the uniformity of the seed layers from $0.50 \pm 0.15 \mu\text{m}$ to $0.75 \pm 0.25 \mu\text{m}$ (Table 4.2). This is consistent with XRD results in terms of both the increasing intensities of (202) ETS-10 peak relative to the ITO peak at $\sim 35.2^\circ$ 2θ , and the decreasing degree of a(b)-out-of-plane preferred crystal orientation (decreasing $\text{CPO}_{(200)/(105)}$ values) in the seed layers deposited using more dip coating steps (vide supra, Figure 4.8 c–e and Table 4.2). The latter result can be explained by the larger on average number of layers of crystals in the thicker seed layers, the higher surface roughness of the intermediate crystal layers compared to the bare ITO glass substrate (Figures 4.9 b, d and f), and the fact that the surface roughness in the crystal multilayers prepared by coating is propagated and amplified with each coating step [44].

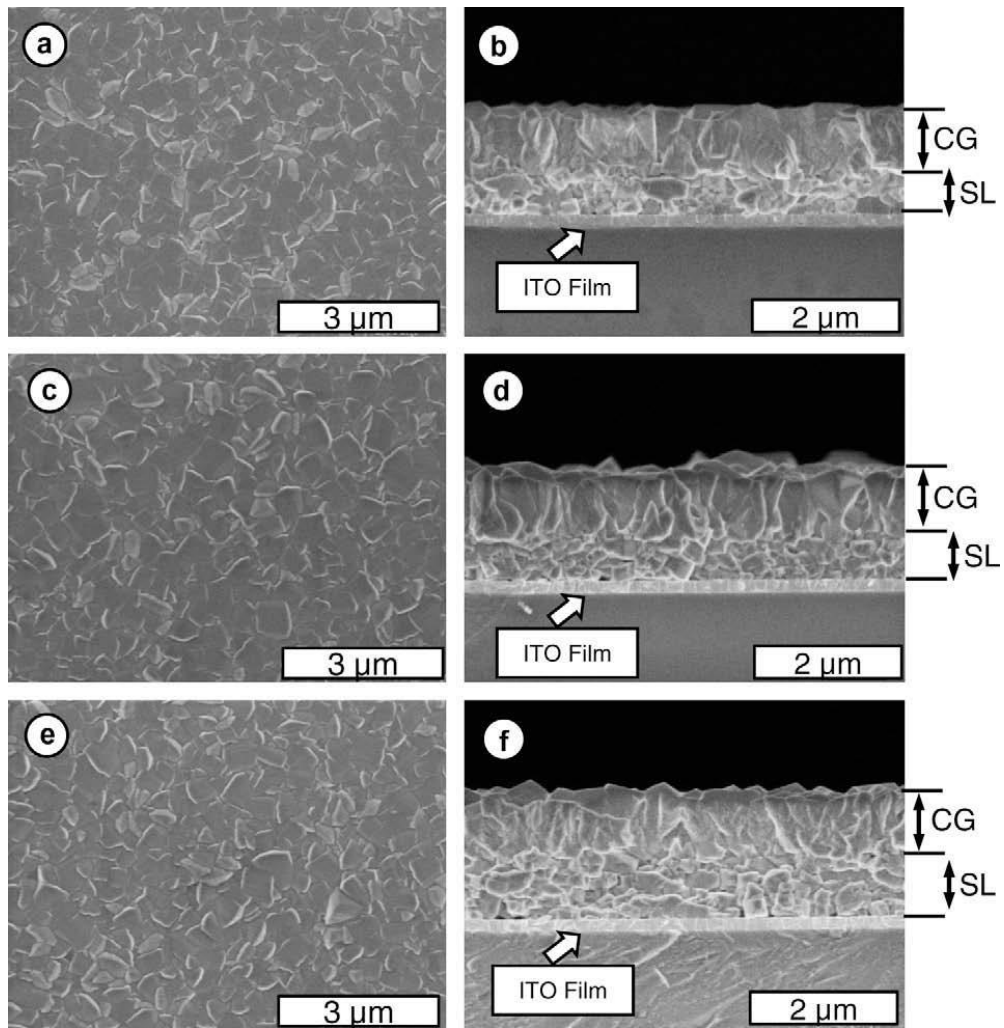


Figure 4.9: FE-SEM top view (a, c, e) and cross-section (b, d, f) images of ETS-10 films prepared on the ITO glass substrates using secondary growth of seed layers deposited using 1 (a, b), 2 (c, d), and 3 (e, f) dip coating steps. *SL = seed layer, CG = columnar grains.

The film columnar grain microstructures with the size of grains increasing from their bottom to the top (Figures 4.9 b, d and f), larger in plane grain dimensions on the top film surfaces compared to those of crystals in the seed layers (Figures 4.9 a, c, e, and Figure 4.4), and a sharper texture in films than in seed layers (Table 4.2), suggest that the geometric selection due to the competitive growth of adjacent seed crystals according to the van der Drift growth model [25, 45, 47–49] played a major role in the ETS-10 film development on the ITO glass substrates. In this faceted growth model, each crystal grows with facets moving with their characteristic normal growth rates until a facet meets the face of adjacent growing crystal. As the immobile grain boundary is formed upon adjacent crystals impingement, the crystals whose orientation is such that the fastest growing direction is perpendicular to the substrate will outgrow the neighboring crystals with other orientations. This implies that during the secondary growth step, the ETS-10 crystals on the surface of the seed layers grow directly by epitaxy. Epitaxy refers to the method of depositing a monocrystalline film on a monocrystalline substrate [55].

The deposited film is denoted as epitaxial film or epitaxial layer. Because the substrate acts as a seed crystal, the deposited film takes on a lattice structure and orientation identical to those of the substrate. This is different from other thin-film deposition methods which deposit polycrystalline or amorphous films, even on single-crystal substrates [55]. No evidence of primary or secondary nucleation of new crystals was observed throughout the columnar grains in films. The absence of these nucleation mechanisms in the mixture used in the secondary growth step was also inferred from the absence of bulk ETS-10 crystallization after a 4-h hydrothermal treatment of this growth mixture with and without seeded ITO substrates placed in the autoclaves. Since the mixture used in the secondary growth step produces a fully crystalline ETS-10 product in a 2-day unseeded crystallization, and thus provides the supersaturation levels adequate for primary nucleation of ETS-10 to occur; the results shown in Figure 4.9 indicate that the

experimental conditions used in this investigation effectively decoupled the nucleation of new crystals from the growth of the seed crystals.

Unlike the films grown on ITO glass, the films prepared on regular glass and quartz peeled off the substrate during drying. ETS-10 film grown on the ITO glass was ultrasonicated in deionized water for up to 60 min, and there were no discernible differences in the substrate coverage with film for the test duration. This result is similar to the results of Yoon and co-workers [21], who, using the secondary growth method were able to prepare zeolite Y films, which were more strongly attached on the ITO glass than on regular glass and fused silica substrates. Accordingly, the reason for stronger bonding of zeolite/zeotype films to the ITO surface than to the glass/fused silica surfaces may be related more to the physical (e.g., contact area between crystals and the substrate) than the chemical (i.e., crystal/substrate surface termination) nature of the crystal/substrate interface. When not completely covered with ETS-10 crystals covalently bonded to the fiber surface, fused silica fibers partially dissolved upon hydrothermal treatment in the secondary growth mixture, and crystals fell off the fibers [17]. This suggests the chemical inertness of ITO may have also played a role in the formation of intact ETS-10 films on the ITO glass surface in this investigation. The Si/Ti ratio measured by EDX for seed crystals in a powder form (5.1 ± 0.1) was identical within the experimental error with the Si/Ti ratio for the columnar grains in films grown from seed layers deposited via triple dip coating (5.3 ± 0.6). Since these Si/Ti values are in good agreement with the theoretical Si/Ti ratio of 5 in ETS-10 [43].

4.3 Preparation of ETS-10 Containing Silver Nanoparticles

4.3.1 Characterization of ETS-10 after Silver Ion-exchange and Reduction

ETS-10 in as-prepared and silver modified forms have been characterized using, X-ray powder diffraction, ICP-OES, SEM, HR-TEM, N₂ Adsorption, XPS, and UV/VIS spectroscopy.

4.3.1.1 X-Ray Diffraction (XRD) Analysis

ETS-10 crystals were synthesized using the molar composition: 3.4 Na₂O:1.5 K₂O: TiO₂: 5.5 SiO₂: 150 H₂O [40]. Cation exchange-capacity of ETS-10 crystals was calculated from theoretical stoichiometry of ETS-10: (Na₂K₂) Ti Si₅ O₁₃ [56] and were found 6.69 meq/g (i.e., 7.22 %). Based on the calculation, 10 % ion-exchange (4.12 mM AgNO₃ solution) was considered sufficient amount for ion-exchange to prevent crystals from structural collapse and formation of silver oxide. In order to figure out the framework stability of crystals 93% (0.5 M AgNO₃ solution) ion-exchange was carried out. ICP-OES analysis indicates that (Table 4.3) for over exchanged sample (93%) Ag concentration was 25.83±0.33 % which was quite above the theoretical value of cation exchange-capacity (7.22%). On the other hand, for 10% ion-exchanged sample, even if final Ag concentration was above the value calculated from cation exchange-capacity, there was no framework damage and silver oxide formation which was proved by XRD analysis, as well. 2θ degrees at 31.3° and 33.8° in the XRD patterns shown in Figure 4.10 (93%-Ag⁺-ETS-10 in blue), belong to the silver oxide (AgO_x)

particle formations, which is in correlation with what was also observed in previous studies [57] (Figure 4.10).

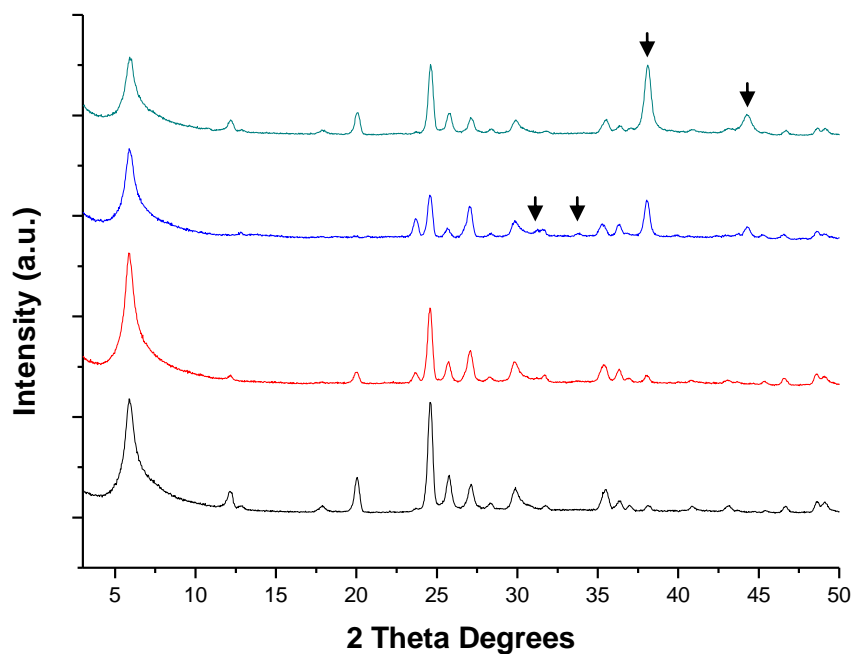


Figure 4.10: XRD patterns of as-synthesized ETS-10 (black), 10%-Ag⁺-ETS-10 (red), 93%-Ag⁺-ETS-10 (blue), Ag⁰-ETS-10 (green).

In the XRD peaks at specific values of 2θ values of as-synthesized sample and silver ion-exchanged samples, relative intensities change significantly. Upon ion-exchange with various ion-exchange percentages some of the 2θ values decreases (20.0°), some of them increases (24.0 , 27.1 , 36.5 and 38.2°). This XRD results indicate that ion-exchange occurred with site selectivity since all the 2θ values belong to specific plane orientation in the ETS-10 structure. To form 3D pore structure through 12-membered and 7-membered ring channels in ETS-10

structure, corner-sharing TiO_6 octahedra connected to each other by tetrahedral SiO_4 . In the Na form of ETS-10, the Na cations fill two nonequivalent positions: one has 8-coordinating oxygen atoms, the other has coordination to 5 oxygen atoms [57, 114].

In the XRD result of Ag^0 -ETS-10 sample, the diffraction peaks at 38° and 44° 2θ degrees (Figure 4.10-green), which were attributed to Ag(111), Ag(200) phases, respectively, suggest existence of metallic silver [115]. On the other hand, even if over exchanged sample was not reduced, it showed metallic silver peaks as well. These peaks could be attributed to existence of metallic silver in over exchanged sample which was also shown in the previous study [57].

4.3.1.2 Scanning Electron Microscopy (SEM)

The SEM images of the ETS-10 containing silver nanoparticles (Figure 4.11) show that there were only crystals in the typical truncated bipyramid morphology of ETS-10 as known from previous studies [40]. SEM images also showed that there was no bulk metal created larger than 20-25 nm in size at the external surface of the ETS-10 crystals. The XRD patterns showed that there were no structural collapse in the structure of ETS-10 upon ion-exchange and reduction, these results can also be observed from the SEM images of Ag^0 -ETS-10 (Figure 4.11-b). Although there were some silver nanoparticles outer surface of the crystals, as can be seen from Figure 4.11-b there was no silver nanoparticle formation on each individual ETS-10 crystal.

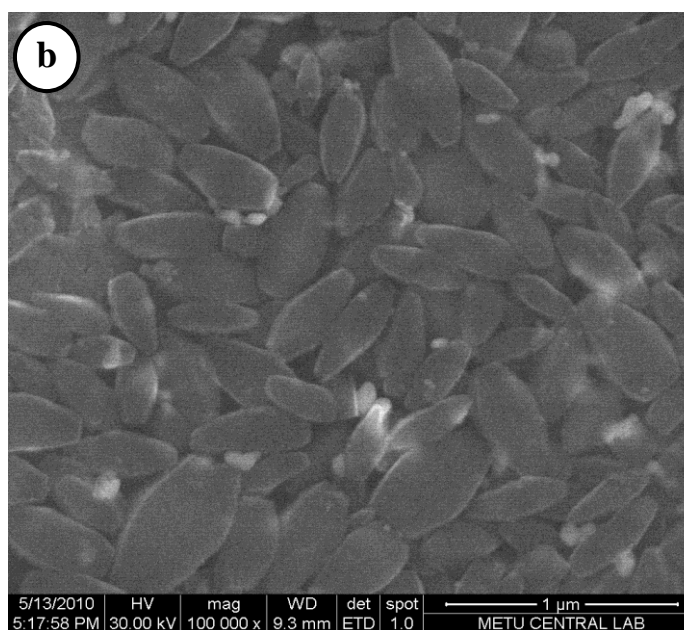
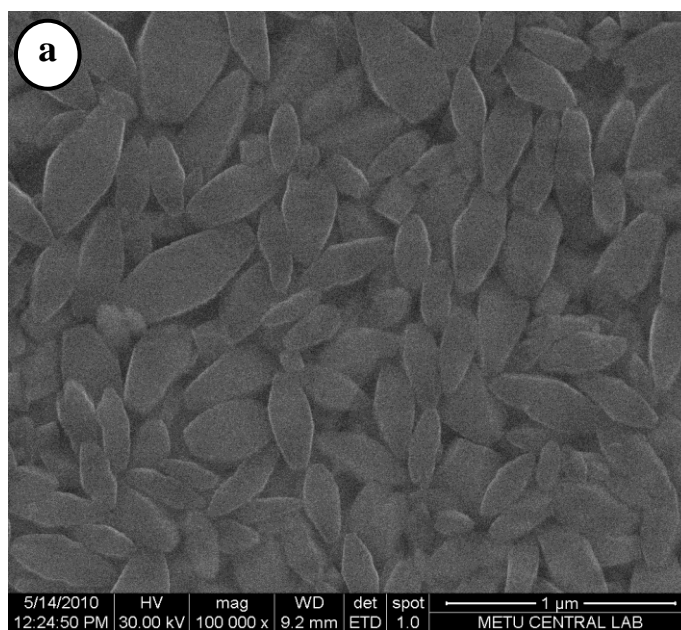


Figure 4.11: SEM images of as-synthesized ETS-10 (a) and ETS-10 containing silver nanoparticles (b).

4.3.1.3 Inductively Coupled Plasma-Optical Emission Spectrometry (ICP-OES)

ICP-OES analysis indicates that (Table 4.3) for over-exchanged sample (93%) Ag concentration was 25.83 ± 0.33 % which was quite above the theoretical value of cation exchange-capacity (7.22%). On the other hand, for 10% ion-exchanged sample even if final Ag concentration was above the value calculated from cation exchange-capacity, there was no framework damage and silver oxide formation which was proved by XRD analysis, as well. Furthermore, ICP-OES analysis indicates that upon ion-exchange with Ag cations, Na positions appear to be preferred over K ones.

Table 4.3: ETS-10 and Ag-ETS-10 Samples and Their Corresponding Na (%), K (%) and Ag (%) Concentration Obtained from ICP-OES Analysis.

Samples	Na (%)	K (%)	Ag (%)
ETS-10	5.56 ± 0.31	3.35 ± 0.12	-
93%-Ag⁺-ETS-10	0.022 ± 0.001	0.022 ± 0.001	25.83 ± 0.33
10%-Ag⁺-ETS-10	3.16 ± 0.07	2.56 ± 0.03	8.18 ± 0.05
Ag⁰-ETS-10	4.88 ± 0.05	1.66 ± 0.01	9.03 ± 0.01

4.3.1.4 UV-VIS Spectroscopy

Figure 4.12 shows the UV-vis absorption spectra of as-synthesized ETS-10 (black), and silver ion-exchanged ETS-10 (Ag^+ -ETS-10) (red). No absorption band between 400 and 800 nm can be observed on sample Ag^+ -ETS-10 when compared with as-synthesized ETS-10. Although ion-exchanged samples were protected from light, there was a broad band between 400-700 nm which could be attributed to small amount of silver nanoparticles inside the ion-exchanged samples.

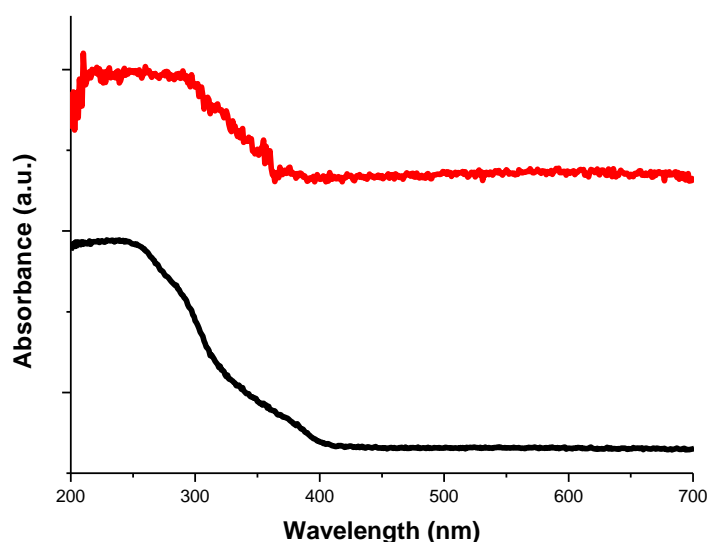


Figure 4.12: UV-VIS spectra of as-synthesized ETS-10 (black), 10 % silver ion-exchanged ETS-10 (red).

As known from the literature [52, 53, 54] pure silver nanoparticles (22 nm nanodots) have surface plasmon band at 400 nm. In this study, UV-Vis spectra of ETS-10 containing silver nanoparticles was also measured as shown in Figure 4.13.

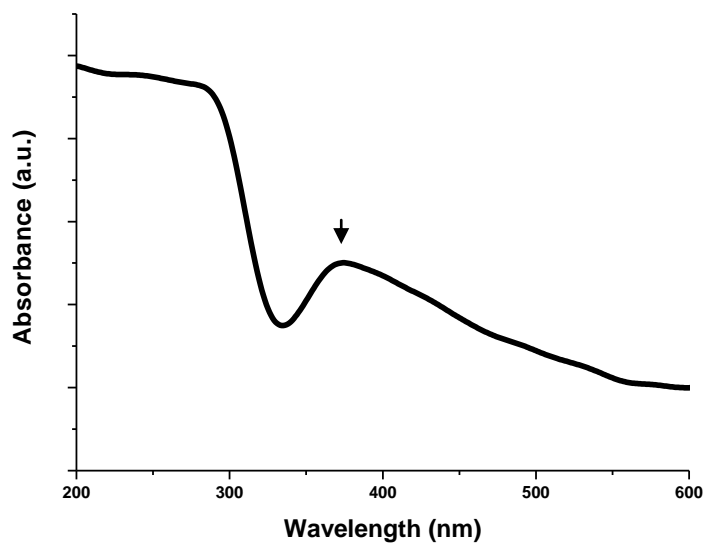


Figure 4.13: UV-Vis spectra of ETS-10 containing silver nanoparticles.

Ag^0 -ETS-10 samples showed distinct absorbance in the visible range centered at ~ 374 nm after reduction as can be seen from Figure 4.13. This result suggests that Ag^0 -ETS-10 samples contain silver nanoparticles. It is well known that surface plasmon resonance is affected by size, shape, and dielectric constant of nanoparticles [53-54]. The shift observed in the surface plasmon resonance could be attributed to the small size of the silver nanoparticles that ETS-10 crystals contain.

4.3.1.5 X-Ray Photoelectron Spectroscopy (XPS)

XPS spectra of Ag⁰-ETS-10 were taken in order to see whether the reduction of silver ions indeed occurred or not. In the literature [120] two typical binding energies are observed for silver metal which are 368.3 eV for 3d_{5/2} and 374.3 eV for 3d_{3/2} ($\Delta = 6.0$ eV). Furthermore, two characteristic binding energies (368.2 eV for 3d_{5/2} and 374.3 eV for 3d_{3/2}, $\Delta = 6.1$ eV) were observed for ETS-10 containing silver nanoparticles [98]. In the current study, the X-ray photoelectron spectra (XPS) of ETS-10 containing silver nanoparticles (Ag⁰-ETS-10) is given in Figure 4.14.

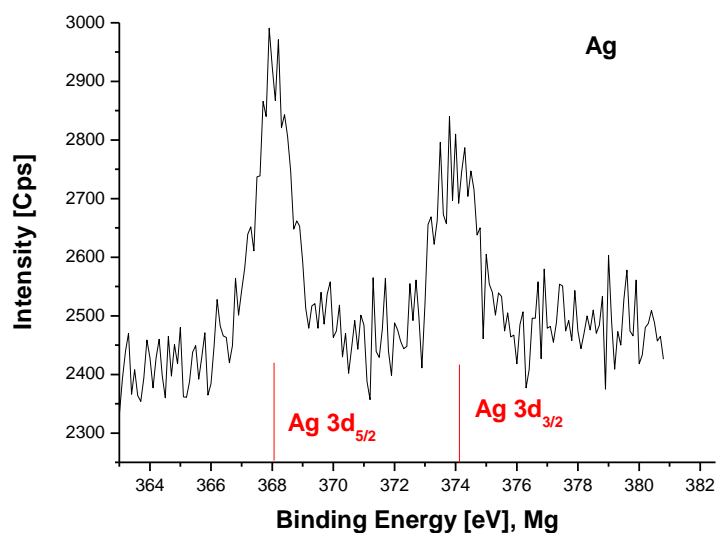


Figure 4.14: XPS spectra of ETS-10 containing silver nanoparticles.

It showed binding energies (BEs) of 368.1 eV and 374.1 eV for Ag 3d_{5/2} and Ag 3d_{3/2}, respectively ($\Delta = 6.0$ eV) [88-89]. According to the data is given in the literature, the current results suggest successful reduction of Ag⁺ to Ag⁰

4.3.1.6 Surface and Pore Size Analysis

There are several reports concerned with the specific surface areas of the ETS-10 samples as shown in Table 4.4. Specific surface area of ETS-10 measured with the technique called BET (Brunauer, Emmett, and Teller). BET theory is a rule for the physical adsorption of gas molecules on a solid surface and serves as the basis for an important analysis technique for the measurement of the specific surface area of a material [119].

Table 4.4 Specific Surface Areas of the ETS-10 Samples.

Specific Surface Area of ETS-10 [m²/g]	Literature Report
235	[61]
255	[58]
258	[60]
269	[59]
365.2	[62]
402	[57]
414	[63]

Table 4.5 shows that the ETS-10 sample had a BET surface area of 406.8 m²/g, and 185.7 m²/g external surface area. There is a decrease in the BET surface area (317.8 m²/g, Ag⁰-ETS-10) upon ion exchange and reduction. “This reduction can be related to both the Pauli radius of Ag cations (0.126 versus 0.095 nm for Na⁺) and some structural collapse [57].”

Table 4.5: Texture Characterization Results of ETS-10 and Ag⁰-ETS-10.

Sample	^a V [cm ³ /g]	S _{BET} [m ² /g]	S _{EXTERNAL} [m ² /g]	S _{INTERNAL} [m ² /g]	^b Mean Pore Width [nm]
ETS-10	0.093	406.8	185.7	221.1	1.07
Ag ⁰ -ETS-10	0.062	317.8	176.6	141.2	0.93

^a t-Method micro pore volume.

^b SF Method pore diameter.

Once ion-exchange is done with extra framework cations of zeolites or zeo-type materials, size and shape of the silver nanoparticles, formed inside after reduction, depend on cage or channel structures of these materials. Metal nanoparticles form inside the pores of zeolite or the channels of zeo-type material. When ions exchanged, ETS-10 materials typically lose their internal surface area. The decrease in surface area increases with the size of the exchanged cations [57]. It can be seen from Table 4.5 internal surface area of Ag⁰-ETS-10 decreased when compared with as-synthesized sample. It would also suggest that there was silver nanoparticle formation inside the ETS-10 after reduction of Ag⁺ to Ag⁰.

4.3.1.7 Transmission Electron Microscopy (TEM)

Transmission electron microscopy images were taken in order to see whether the reduction of silver ions made framework damages or not. Figure 4.15 shows the high resolution transmission electron microscopy (HR-TEM) images of ETS-10 containing silver nanoparticles. The lines indicate the framework of ETS-10 (Si, O, Ti, K, Na).

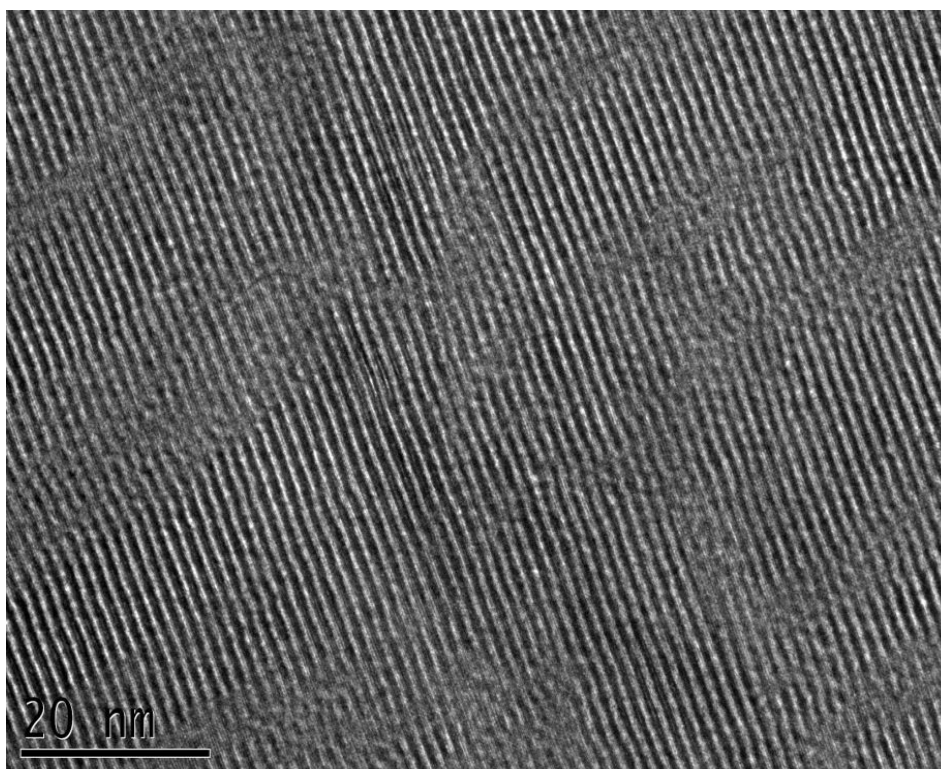


Figure 4.15 TEM image of ETS-10 containing silver nanoparticles.

This image showed that there were no framework damages after ion-exchange and reduction. Furthermore, high resolution TEM image indicates that there was no significant amount of silver nanoparticles at the outer surface of each individual ETS-10 crystals as shown in the Figure 4.16. In the literature when metal nanoparticles incorporated into the porous materials darker parts attributed to these nanoparticles [98]. Dark area inside the red circle could be attributed to the silver nanoparticles at the outer surface of the ETS-10.

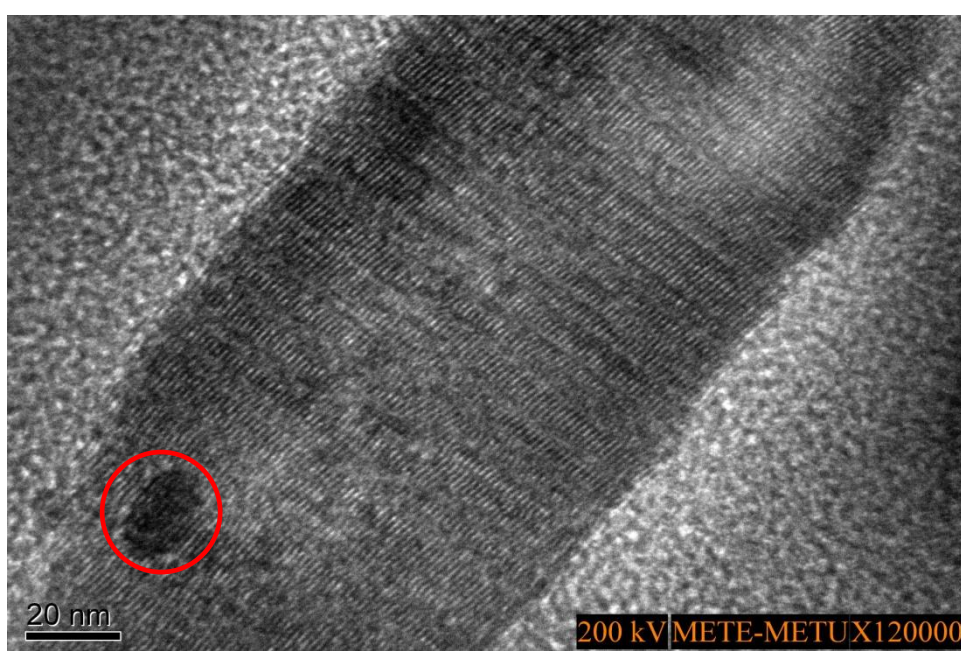


Figure 4.16 TEM image of ETS-10 containing silver nanoparticles.

On the other hand, as also observed from SEM image of Ag^0 -ETS-10, there were some silver nanoparticles on the external surface of the ETS-10 (Figure 4.11-b). This formation was probably due to the reduction process of Ag^+ ions. Since reduction process was carried out in liquid media with sodium borohydride, excess silver ions in water also reduced to silver nanoparticles. These silver

nanoparticles were probably attached on ETS-10 after washing and drying step. Since they attached loosely on ETS-10 crystals, in order to minimize this formation, samples were washed a lot with 1000 mL deionized water. ICP-OES analysis (Table 4.3) of Ag⁰-ETS-10 could also be the proof of this formation on the surface because in 10% -Ag⁺-exchanged sample Ag content was 8.18±0.05%; however, in Ag⁰-ETS-10 it was 9.03±0.01%. The increase in Ag content might be due to the silver formation on the surface.

4.3.1.8 Transmittance-Reflectance Measurements

In order to understand how light interacts with the prepared samples, transmittance and reflectance measurements were carried out. Figure 4.17-a and 4.17-b show reflectance and transmittance measurements of prepared samples on ITO glass, respectively. According to Figure 4.17, the reflectance and transmittance values of ETS-10 were observed to be higher than Ag⁰-ETS-10 samples. In reflectance measurements, the reflectance data of 1-time dip coated ETS-10 (Figure 4.17-a-black) was higher than 1-time dip coated Ag⁰-ETS-10 (Figure 4.17-a-green). This was also observed for 2-times dip coated ETS-10 (Figure 4.17-a-red) vs. 2-times dip coated Ag⁰-ETS-10 (Figure 4.17-a-pink) and 3-times dip coated ETS-10 (Figure 4.17-a-blue) vs. 3-times dip coated Ag⁰-ETS-10 (Figure 4.17-a-brown).

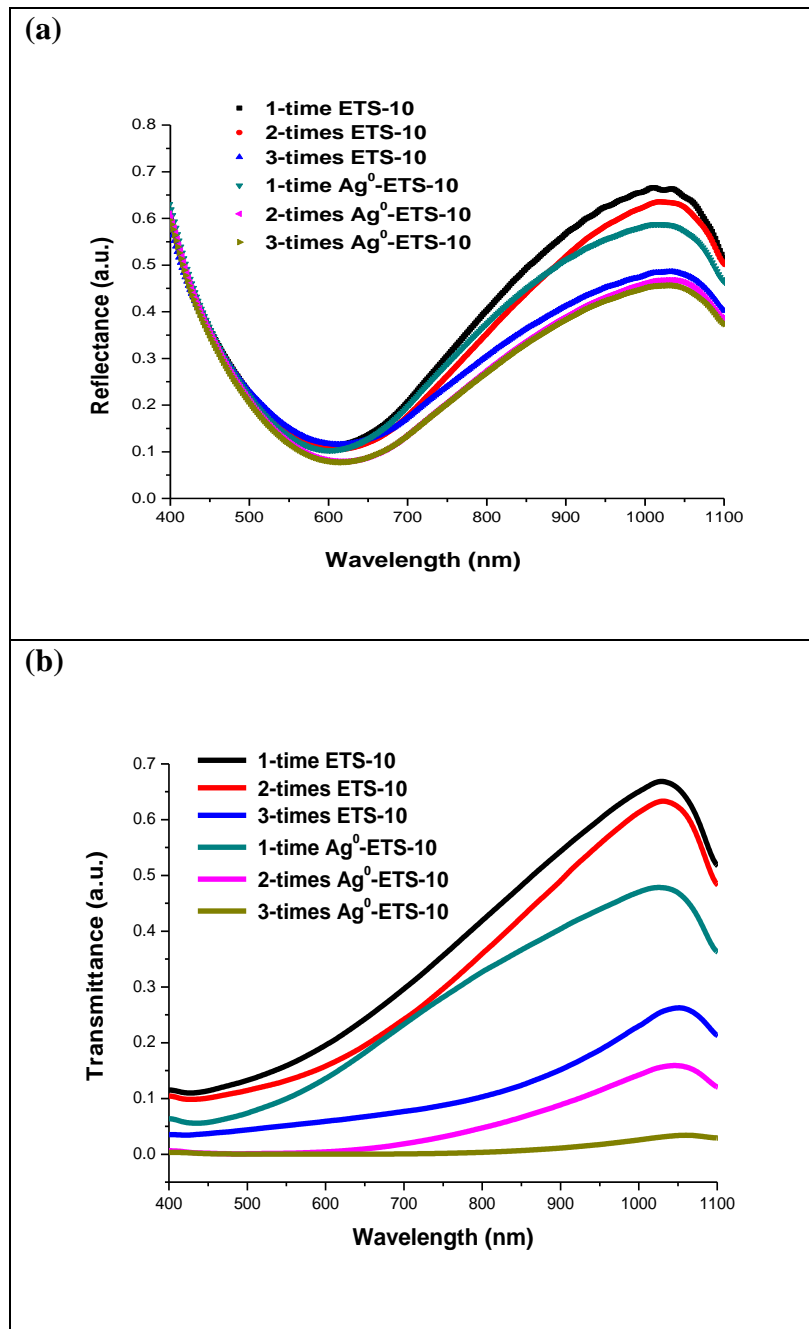


Figure 4.17: **(a)** Reflectance data of ETS-10 and Ag⁰-ETS-10 samples dip-coated on ITO glass. 1-time (black), 2-times (red), 3-times (blue) dip-coated ETS-10; 1-time (green), 2-times (pink), 3-times (brown) dip-coated Ag⁰-ETS-10. **(b)** Transmittance data of ETS-10 and Ag⁰-ETS-10 samples dip-coated on ITO glass. 1-time (black), 2-times (red), 3-times (blue) dip-coated ETS-10; 1-time (green), 2-times (pink), 3-times (brown) dip-coated Ag⁰-ETS-10.

In transmittance measurements, the transmittance data of 1-time dip coated ETS-10 (Figure 4.17-b-black) was higher than 1-time dip coated Ag⁰-ETS-10 (Figure 4.17-b-green). This was also observed for 2-times dip coated ETS-10 (Figure 4.17-b-red) vs. 2-times dip coated Ag⁰-ETS-10 (Figure 4.17-b-pink) and 3-times dip coated ETS-10 (Figure 4.17-b-blue) vs. 3-times dip coated Ag⁰-ETS-10 (Figure 4.17-b-brown). This may suggest that the ETS-10 samples have lower absorbance than the Ag⁰-ETS-10 samples. This would indicate that silver nanoparticle incorporation into ETS-10 samples increases the absorption of light with respect to the regular ETS-10 samples.

However, these data may arise from the ITO layer on glass. In order to figure out whether the same results were going to be obtained without ITO, same samples were prepared on quartz, as well. The transmittance and reflectance results are shown in Figure 4.18. In reflectance measurements, the reflectance data of 1-time dip coated ETS-10 (Figure 4.18-a-black) was higher than 1-time dip coated Ag⁰-ETS-10 (Figure 4.18-a-green). This was also observed for 2-times dip coated ETS-10 (Figure 4.18-a-red) vs. 2-times dip coated Ag⁰-ETS-10 (Figure 4.18-a-pink) and 3-times dip coated ETS-10 (Figure 4.18-a-blue) vs. 3-times dip coated Ag⁰-ETS-10 (Figure 4.18-a-brown). In transmittance measurements, the transmittance data of 1-time dip coated ETS-10 (Figure 4.18-b-black) was higher than 1-time dip coated Ag⁰-ETS-10 (Figure 4.18-b-green). This was also observed for 2-times dip coated ETS-10 (Figure 4.18-b-red) vs. 2-times dip coated Ag⁰-ETS-10 (Figure 4.18-b-pink) and 3-times dip coated ETS-10 (Figure 4.18-b-blue) vs. 3-times dip coated Ag⁰-ETS-10 (Figure 4.18-b-brown). These results indicate that reflectance and transmittance values of ETS-10 samples were higher than ETS-10 containing silver nanoparticles samples. The same trend was also observed on quartz which again indicates that silver nanoparticle incorporation into ETS-10 samples increases the absorption of light with respect to the regular ETS-10 samples.

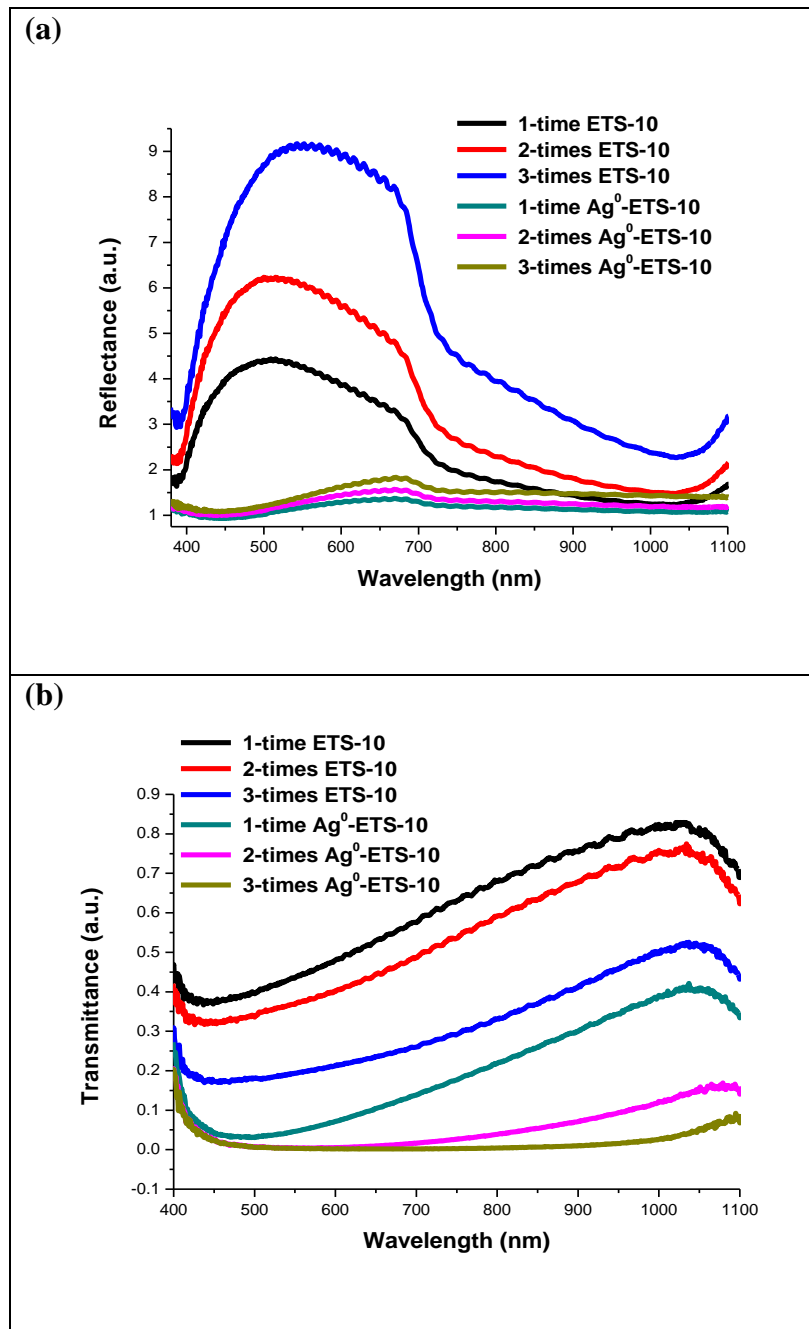


Figure 4.18: **(a)** Reflectance data of ETS-10 and Ag⁰-ETS-10 samples dip-coated on quartz. 1-time (black), 2-times (red), 3-times (blue) dip-coated ETS-10; 1-time (green), 2-times (pink), 3-times (brown) dip-coated Ag⁰-ETS-10. **(b)** Transmittance data of ETS-10 and Ag⁰-ETS-10 samples dip-coated on quartz. 1-time (black), 2-times (red), 3-times (blue) dip-coated ETS-10; 1-time (green), 2-times (pink), 3-times (brown) dip-coated Ag⁰-ETS-10.

It seems from the rest of the characterization results that the obtained silver particles are both in the channels and also on the external surface of Ag⁰-ETS-10. At this point, the relative quantities of the silver particles formed inside and outside is not figured out. However, as explained in Section 4.3.1.7 (TEM), it can be hypothesized that there was no significant amount of silver nanoparticles on the surface of each individual ETS-10 crystals.

The size of silver nanoparticles inside ETS-10 should be less than 1 nm due to the framework structure of ETS-10 where the pore diameters are ~0.8 nm. However, the size of the silver particles on the external surface of ETS-10 was observed to be approximately 20-25 nm from the SEM and TEM images. The size of the formed silver particles in relation with the reduction process is important, because the absorption and scattering of these particles depend on the polarizability and the size of the particle as explained by Mie Theory (eqn. 4.2),

$$\alpha = 4\pi a^3 \frac{\varepsilon - \varepsilon_m}{\varepsilon + 2\varepsilon_m} \quad (4.2)$$

where α is polarizability, a is radius of the sphere particle, ε and ε_m are the dielectric constants of the sphere and medium. Therefore, depending on the light being scattered or absorbed, it can be defined by scattering (C_{sca}) and absorption (C_{abs}) cross sections, which are shown in Equations 4.3 and 4.4.

$$C_{\text{abs}} = k\text{Im}[\alpha] = 4\pi k a^3 \text{Im} \left[\frac{\varepsilon - \varepsilon_m}{\varepsilon + 2\varepsilon_m} \right] \quad (4.3)$$

$$C_{\text{sca}} = \frac{k^4}{6\pi} |\alpha|^2 = \frac{8\pi}{3} k^4 a^6 \left| \frac{\varepsilon - \varepsilon_m}{\varepsilon + 2\varepsilon_m} \right|^2 \quad (4.4)$$

As shown in the above equations, both absorption and scattering abilities of particles increase with increasing particle size. However, the tendency for the scattering ability of particles is higher than the absorption ability (a^6 versus a^3 , where a is radius of the sphere). These two equations were found to be equal for silver nanoparticles to each other for $a \cong 34$ nm [118]. For particles with $a < 34$ nm, the ability of the silver nanoparticles for absorbance is higher than their ability for scattering. In the current study, it seems like the formed silver nanoparticles are less than 34 nm after reduction, and thus the absorption of the silver nanoparticles in the Ag^0 -ETS-10 will most likely be dominant when compared with the scattering from these silver nanoparticles.

CHAPTER 5

CONCLUSIONS

Secondary growth of the seed crystals with the highly anisotropic shapes and submicrometer sizes was used to prepare a(b)-out-of-plane oriented ETS-10 thin films (average thickness smaller than $\sim 2 \mu\text{m}$) on the conductive and transparent ITO glass substrates. Since the main channels and quantum wires run along ETS-10 crystal a and b directions [32, 43], this orientation should dominate (mass, electrical) transport across the films. The secondary growth conditions employed effectively decoupled nucleation from crystal growth so that the seed crystals at the surface of seed layers grew directly by epitaxy. Columnar film microstructure, the increase of the in-plane grain size with increasing film thickness and sharpening of film texture after secondary growth suggested that the adjacent seed crystals at the surface of the thickening film grew according to the evolutionary van der Drift growth mechanism. It is hypothesized that this self-orienting growth of the seed crystals was achieved due to the anisotropy of ETS-10 crystal growth and high packing density of crystals in the seed layers. The prepared films retained integrity after a 60-min substrate sonication in water; this suggests strong film bonding to the ITO glass substrates. It is believed that the ability to grow oriented ETS-10 films on the ITO glass substrates will open new directions for investigations of ETS-10 in advanced applications.

In order to make a preliminary study to incorporate nanoparticles in a unique material such as ETS-10, silver nanoparticle modified ETS-10 crystals were prepared and characterized in detail to investigate the interaction of silver nanoparticles with the synthesized ETS-10 crystals. XRD patterns of ion-exchanged ETS-10 crystals at certain concentrations showed that there was no structural collapse and silver oxide formations upon the formation of silver nanoparticles. XPS and TEM analysis suggested the formation of silver nanoparticles at the external and internal surfaces of ETS-10. Furthermore, UV-Vis spectroscopy showed that after reduction there was an absorption band in the visible range, which indicates silver nanoparticle formation, as well. In order to study the optical properties of the silver modified ETS-10, transmittance-reflectance measurements were carried out. The optical results showed that silver nanoparticles in the Ag⁰-ETS-10 will most likely be dominant when compared with the scattering from these silver nanoparticles. Although some hypothetical conclusions can be drawn from these preliminary studies, further detailed studies, especially using the ETS-10 thin films prepared according to the current thesis study, are necessary to make definitive conclusions.

REFERENCES

- [1] P. Payra, P.K. Dutta, in: S.M. Auerbach, K.A. Carrado, P.K. Dutta (Eds.), Handbook of Zeolite Science and Technology, Marcel Dekker, Inc., New York, 2003, p. 1.
- [2] B. Zhang, M. Zhou, X. Liu, *Adv. Mater.* 20 (2008) 2183.
- [3] B. Yilmaz, A. Sacco Jr., J. Deng, *Appl. Phys. Lett.* 90 (2007) 152101.
- [4] P. Atienzar, S. Valencia, A. Corma, H. Garcia, *Chem. Phys. Chem.* 8 (2007) 1115.
- [5] G. Guan, T. Kida, K. Kusakabe, K. Kimura, E. Abe, A. Yoshida, *Appl. Catal. A: Gen.* 295 (2005) 71.
- [6] R. Koeppel, O. Bossart, G. Calzaferri, N.S. Sariciftci, *Sol. Energy Mater. Sol. Cells* 91 (2007) 986.
- [7] X. Zhou, T. Yu, Y. Zhang, J. Kong, Y. Tang, J.-L. Marty, B. Liu, *Electro. Chem. Commun.* 9 (2007) 1525.
- [8] T. Yu, Y. Zhang, C. You, J. Zhuang, B. Wang, B. Liu, Y. Kang, Y. Tang, *Chem. Eur. J.* 12 (2006) 1137.
- [9] A. Corma, H. Garcia, *Chem. Commun.* 10 (2004) 1443.
- [10] S. Anandan, M. Yoon, *J. Photochem. Photobiol. C: Photochem. Rev.* 4 (2003) 5.
- [11] S.S. Rayalu, N. Dubey, N.K. Labhsetwar, S. Kagne, S. Devotta, *Int. J. Hydrogen Energy* 32 (2007) 2776.
- [12] G. Calzaferri, S. Huber, H. Maas, C. Minkowski, *Angew. Chem. Int. Ed.* 42 (2003) 3732.
- [13] M. Anpo, T.-H. Kim, M. Matsuoka, *Catal. Today* 142 (2009) 114.
- [14] K.B. Yoon, *Acc. Chem. Res.* 40 (2007) 29.
- [15] S. Ozturk, B. Akata, *Micropor. Mesopor. Mater.* 126 (2009) 228.
- [16] M.N. Ismail, T.L. Goodrich, Z. Ji, K.S. Ziemer, J. Warzywoda, A. Sacco Jr., *Micropor. Mesopor. Mater.* 118 (2009) 245.
- [17] Z. Ji, J. Warzywoda, A. Sacco Jr., *Micropor. Mesopor. Mater.* 101 (2007) 279.
- [18] C. Leiggener, G. Calzaferri, *Chem. Phys. Chem.* 5 (2004) 1593.
- [19] F. Cucinotta, Z. Popovic, E.A. Weiss, G.M. Whitesides, L. De Cola, *Adv. Mater.* 21 (2009) 1142.
- [20] K. Ha, J.S. Park, K.S. Oh, Y.-S. Zhou, Y.S. Chun, Y.-J. Lee, K.B. Yoon, *Micropor. Mesopor. Mater.* 72 (2004) 91.
- [21] H.S. Kim, M.H. Lee, N.C. Jeong, S.M. Lee, B.K. Rhee, K.B. Yoon, *J. Am. Chem. Soc.* 128 (2006) 15070.
- [22] L. Wang, W. Mao, D. Ni, J. Di, Y. Wu, Y. Tu, *Electrochem. Commun.* 10 (2008) 673.
- [23] A.B. Chebotareva, G.G. Untila, T.N. Kost, S. Jorgensen, A.G. Ulyashin, *Thin Solid Films* 515 (2007) 8505.

- [24] S. Nair, M. Tsapatsis, in: S.M. Auerbach, K.A. Carrado, P.K. Dutta (Eds.), *Handbook of Zeolite Science and Technology*, Marcel Dekker, Inc., New York, 2003, p. 867.
- [25] B. Yilmaz, K.G. Shattuck, J. Warzywoda, A. Sacco Jr., *Chem. Mater.* 18 (2006) 1107.
- [26] N.C. Jeong, M.H. Lee, K.B. Yoon, *Angew. Chem. Int. Ed.* 46 (2007) 5868.
- [27] S. Uma, S. Rodrigues, I.N. Martyanov, K.J. Klabunde, *Micropor. Mesopor. Mater.* 67 (2004) 181.
- [28] M.J. Nash, S. Rykov, R.F. Lobo, D.J. Doren, I. Wachs, *J. Phys. Chem. C* 111 (2007) 7029.
- [29] F.X. Llabrés i Xamena, P. Calza, C. Lamberti, C. Prestipino, A. Damin, S. Bordiga, E. Pelizzetti, A. Zecchina, *J. Am. Chem. Soc.* 125 (2003) 2264.
- [30] Y. Shiraishi, D. Tsukamoto, T. Hirai, *Langmuir* 24 (2008) 12658.
- [31] S.M. Kuznicki, US Patent 4, 853, 2002, 1989.
- [32] M.W. Anderson, O. Terasaki, T. Ohsuna, A. Philippou, S.P. MacKay, A. Ferreira, J. Rocha, S. Lidin, *Nature* 367 (1994) 347.
- [33] E. Borello, C. Lamberti, S. Bordiga, A. Zecchina, C.O. Arean, *Appl. Phys. Lett.* 71 (1997) 2319.
- [34] H.K. Jeong, J. Krohn, K. Sujaoti, M. Tsapatsis, *J. Am. Chem. Soc.* 124 (2002) 12966.
- [35] Z. Lin, J. Rocha, A. Navajas, C. Téllez, J. Coronas, J. Santamaría, *Micropor. Mesopor. Mater.* 67 (2004) 79.
- [36] Z. Lin, J.P. Rainho, J. Domingues, L.D. Carlos, J. Rocha, *Micropor. Mesopor. Mater.* 79 (2005) 13.
- [37] I. Tiscornia, Z. Lin, J. Rocha, C. Téllez, J. Coronas, J. Santamaría, in: J. Cejka, N. Zilkova, P. Nachtigall (Eds.), *Molecular Sieves: From Basic Research to Industrial Applications, Studies in Surface Science and Catalysis, Part A*, vol. 158, Elsevier, Amsterdam, 2005, p. 423.
- [38] Z. Lin, J. Rocha, in: R. Xu, Z. Gao, J. Chen, W. Yan (Eds.), *From Zeolites to Porous MOF Materials – The 40th Anniversary of International Zeolite Conference, Studies in Surface Science and Catalysis*, vol. 170, Elsevier, Amsterdam, 2007, p. 493.
- [39] I. Tiscornia, S. Irusta, C. Téllez, J. Coronas, J. Santamaría, *J. Membr. Sci.* 311 (2008) 326.
- [40] L. Lv, F. Su, X.S. Zhao, *Micropor. Mesopor. Mater.* 76 (2004) 113.
- [41] Z. Ji, B. Yilmaz, J. Warzywoda, A. Sacco Jr., *Micropor. Mesopor. Mater.* 81 (2005) 1.
- [42] X. Wang, A.J. Jacobson, *Chem. Commun.* (1999) 973.
- [43] M.W. Anderson, O. Terasaki, T. Ohsuna, P.J.O. Malley, A. Philippou, S.P. MacKay, A. Ferreira, J. Rocha, S. Lidin, *Philos. Magn. B* 71 (1995) 813.
- [44] J. Kobler, H. Abrevaya, S. Mintova, T. Bein, *J. Phys. Chem. C* 112 (2008) 14274.
- [45] A. Gouzinis, M. Tsapatsis, *Chem. Mater.* 10 (1998) 2497.
- [46] Z. Ji, J. Warzywoda, A. Sacco Jr., *Micropor. Mesopor. Mater.* 109 (2008) 1.
- [47] G. Xomeritakis, S. Nair, M. Tsapatsis, *Micropor. Mesopor. Mater.* 38 (2000) 61.

- [48] C.V. Thompson, *Annu. Rev. Mater. Sci.* 30 (2000) 159.
- [49] P. Smereka, X. Li, G. Russo, D. J Srolowitz, *Acta Mater.* 53 (2005) 1191
- [50] N. C. Jeong, M. H. Lee, K. B. Yoon, *Angew. Chem. Int. Ed.* 46 (2007) 5868 –5872
- [51] V. Valtchev, S. Mintova, M. Tsapatsis, *Ordered Porous Solids: Recent Advances and Prospects*, First Edition; Elsevier B.V., Oxford, 2009, p 64
- [52] S. Link, M. A. El-Sayed, *Annu. Rev. Phys. Chem.* 54 (2003) 331–366
- [53] D. D. Evanoff Jr. and G. Chumanov, *ChemPhysChem* 6 (2005)1221 – 1231
- [54] D. D. Evanoff, Jr. and G. Chumanov, *J. Phys. Chem. B* 108 (2004) 13957-13962
- [55] <http://en.wikipedia.org/wiki/Epitaxy> (last visited on 23 March 2010)
- [56] L. Lv., F. Su, X. s. Zhao, *J. of Porous Mater.* (2006), 13, 263-267
- [57] I. Tiscornia, S. Irusta, P. Pradanos, C. Tellez, J. Coronas, and J. Santamaria, *J. Phys. Chem. C* 2007, 111, 4702-4709
- [58] G. Guan, T. Kida, K. Kusakabe, K. Kimura, E. Abe, A. Yoshida, *Applied Catalysis A: General* 295 (2005) 71–78
- [59] L. Lv, K. Wang, F. Su, X.S. Zhao, *Journal of Colloid and Interface Science* 305 (2007) 218–225
- [60] G. X. S. Zhao, J. L. Lee, and P. A. Chia, *Langmuir* 2003, 19, 1977-1979
- [61] S. Uma, S. Rodrigues, I. N. Martyanov, K. J. Klabunde, *Microporous and Mesoporous Materials* 67 (2004) 181–187
- [62] J. H. Choi, S. D. Kim, Y. J. Kwon, W. J. Kim, *Microporous and Mesoporous Materials* 96 (2006) 157–167
- [63] J. H. Choi, S.D. Kim, S.H. Noh, S.J. Oh, W. J. Kim, *Microporous and Mesoporous Materials* 87 (2006) 163-169
- [64] S. Bhatia, *Zeolite Catalysis: Principles and Applications*, CRC Press, 1990, p 8.
- [65] R. Xu, W. Pang, J. Yu, Q. Huo, J. Chen, *Chemistry of Zeolites and Related Porous Materials: Synthesis and Structure*, Wiley, 2007, p 23.
- [66] S. Link, M. A. El-Sayed, *Int. Reviews in Physical Chemistry*, 2000, Vol. 19, No. 3, 409-453
- [67] A. Henglein, *Chem. Rev.*, 1989, 1861-1873
- [68] P. Mulvaney, *Langmuir*, 1996, 12, 788-800
- [69] K. Esumi, T. Tano, K. Meguro, *Langmuir*, 1989, 5, 268-270
- [70] M. T. Reetz, W. Helbig, *J. Am. Chem. Soc.*, 1994, 116, 7401-7402
- [71] Y. Yu, S. Chang, C. Lee, C. R. C. Wang, *J. Phys. Chem. B*, 1997, Vol. 101, No.34, 6661-6664
- [72] N. Toshima, T. Takahashi, H. Hirai, *Chem. Lett.*, 1985, 1245-1248
- [73] K. Wegner, B. Walker, S. Tsantilis, S. E. Pratsinis, *Chemical Engineering Science*, 2002, 57, 1753-1762
- [74] R. Abargues, J. Marques-Hueso, J. Canet-Ferrer, E. Pedrueza, J. L. Valdes, E. Jimenez, J. P. Martinez-Pastor, *Nanotechnology*, 2008, 19, 355308
- [75] N. A. Hatab, J. M. Oran, M. J. Sepaniak, *ACS Nano*, 2008, Vol. 2, No. 2, 377-385
- [76] J. Marques-Hueso, R. Abargues, J. Canet-Ferrer, J. L. Valdes, J. P. Martinez-Pastor, *Microelectronic Engineering*, 2010, 87, 1147-1149

- [77] M. Zahmakıran, F. Durap, S. Özkar, *International J. of Hydrogen Energy*, 2010, 35, 187-197
- [78] M. Zahmakıran, S. Özkar, *Langmuir*, 2008, 24, 7065-7067
- [79] C. A. Foss, G. L. Hornyak, M. J. Tierney, C. R. Martin, 1992, *J. Phys. Chem.*, 96, 9001.
- [80] G. L. Hornyak, C. J. Patrissi, C. R. Martin, 1997, *J. Phys. Chem. B*, 101, 1548.
- [81] C. A. Foss, G. L. Hornyak, J. A. Stockert, C. R. Martin, 1992, *J. Phys. Chem.*, 96, 7497-7499.
- [82] C. A. Foss, G. L. Hornyak, J. A. Stockert, C. R. Martin, 1994, *J. phys. Chem.*, 98, 2963-2971.
- [83] G. L. Hornyak, C. R. Martin, *Thin Solid Films*, 1997, 303, 84.
- [84] M. B. Mohamed, K. Z. Ismail, S. Link, M. A. El-Sayed, *J. Phys. Chem. B* 1998, 102, 9370-9374
- [85] I. Lisiecki, F. Billoudet, and M. P. Pileni, *J. Phys. Chem.* 1996, 100, 4160-4166
- [86] I. Lisiecki and M. P. Pileni, *J. Am. Chem. Soc.* 1993, 115, 3887-3896
- [87] J. Turkevich, P. C. Stevenson, J. Hillier, *Discuss. Faraday. Soc.* 1951, 11, 55-75.
- [88] I. M. Arabatzis, T. Stergiopoulos, M. C. Bernard, D. Labou, S. G. Neophytides, P. Falaras, *Appl. Catal. B*, 2003, 42, 187.
- [89] B. Xin, L. Jing, Z. Ren, B. Wang, H. Fu, *J. Phys Chem. B*, 2005, 109, 2805.
- [90] X.Liu, J.K. Thomas, *Chem. Commun.*(1996) 1435.
- [91] J.Rocha, A. Ferreira, Z.Lin, M.W.Anderson, *Micropor. and Mesopor.Mater.* 23 (1998) 253.
- [92] Michael J. Nash, Raul F. Lobo, Douglas J. Doren, *Applied Catalysis B: Environmental* 88 (2009) 232–239
- [93] A. Anson, Y.Wang, C.C.H. Lin, T.M. Kuznicki, S.M. Kuznicki, *Chemical Engineering Science* 63 (2008) 4171-4175
- [94] G. Agostini, S. Usseglio, E. Groppo, M. J. Uddin, C. Prestipino, S. Bordiga, A. Zecchina, P. L. Solari, and C. Lamberti, *Chem. Mater.* 2009, 21, 1343–1353
- [95] A. Anson, S. M. Kuznicki, T. Kuznicki, T. Haastrup, Y. Wang, C.H. Lin, J. A. Sawada, E. M. Eyring, D. Hunter, *Micropor. and Mesopor. Mater.* 109 (2008) 577–580
- [96] D. D. Evanoff, Jr., G. Chumanov, *J. Phys. Chem. B.*, 2004, 108, 13957-13962
- [97] A. Anson, S. M. Kuznicki, T. Kuznicki, T. Haastrup, Y. Wang, C.C.H. Lin, J. A. Sawada, E. M. Eyring, D. Hunter, *Micropor. and Mesopor. Mater.* 109 (2008) 577–580
- [98] L. Lv, Y. Luo, W. J. Ng, X.S. Zhao, *Micropor. and Mesopor. Mater.* 120 (2009) 304–309
- [99] E. Borello, C. Lamberti, S. Bordiga, and A. Zecchina, *Appl. Phys. Lett.* 71 (16), 20 October 1997
- [100] N. C. Jeong, Y. J. Lee, J. Park, H. Lim, C. Shin, H. Cheong, and K. B. Yoon, *J. Am. Chem. Soc.* 2009, 131, 13080–13092
- [101] G. X. S. Zhao, J. L. Lee, and P. A. Chia, *Langmuir* 2003, 19, 1977-1979
- [102] V. Luca, M. Osborne, D. Sizgek, C. Griffith, P. Z. Araujo, *Chem. Mater.* 2006, 18, 6132-6138.

- [103] M. J. Nash, R. F. Lobo, D. J. Doren, *Applied Catalysis B: Environmental* 88 (2009) 232–239
- [104] A. Gervasini, C. Picciau, A. Auroux, *Microporous and Mesoporous Materials* 35–36 (2000) 457–469
- [105] S. Galioglu, M. N. Ismail, J. Warzywoda, A. Sacco Jr., B. Akata, *Microporous and Mesoporous Materials* 131 (2010) 401–406
- [106] J. Xu, X. Han, H. Liu, Y. Hu, *Colloids and Surfaces A: Physicochem. Eng. Aspects* 273 (2006) 179–183
- [107] N. Vigneshwaran, R. P. Nachane, R. H. Balasubramanya and P. V. Varadarajan, *Carbohydrate Research* 341 (2006) 2012–2018
- [108] Y. Zhao, Y. Jiang, Y. Fang, *Spectrochimica Acta Part A* 65 (2006) 1003–1006
- [109] S.L. Smitha, K.M. Nissamudeen, D. Philip, K.G. Gopchandran, *Spectrochimica Acta Part A* 71 (2008) 186–190
- [110] D. Basak, S. Karan, B. Mallik, *Chemical Physics Letters* 420 (2006) 115–119
- [111] P. Gangopadhyay, R. Kesavamoorthy, S. Bera, P. Magudapathy, K. G. M. Nair, B. K. Panigrahi, and S.V. Narasimhan, *Physical Review Letters* 94, 047403 (2005)
- [112] J. Gao, J. Fu, C. Lin, J. Lin, Y. Han, X. Yu, and C. Pan, *Langmuir* 2004, 20, 9775-9779
- [113] P.V. Adhyapak, P. Karandikar, K. Vijayamohanam, A.A. Athawale, A.J. Chandwadkar, *Materials Letters* 58 (2004) 1168– 1171
- [114] Wang, X.; Jacobson, A. *Chem. Commun.* 1999, 973.
- [115] L. Lv, Y. Luo, W. J. Ng, X.S. Zhao, *Microporous and Mesoporous Materials* 120 (2009) 304-309
- [116] S. A. Maier, *Plasmonics: Fundamentals and Applications*, Springer, 2007, New York, p.68
- [117] B. M. Weckhuysen, P. Voort, G. Catana, *Spectroscopy of Transition Metal Ions on Surfaces*, Leuven University Press, 2000, p. 222
- [118] Urcan Güler, Middle East Technical University, Physics Department, MSc. Thesis, September 2009, p. 19
- [119] http://en.wikipedia.org/wiki/BET_theory (last visited on 5 July 2010)
- [120] J. F. Moulder, W. F. Stickle, E. Sobol, K. D. Bomben, *Handbook of X-Ray Photoelectron Spectroscopy*, ULVAC-PHI, Inc., Japan, 1995